ZEUS-2D: A RADIATION MAGNETOHYDRODYNAMICS CODE FOR ASTROPHYSICAL FLOWS IN TWO SPACE DIMENSIONS. II. THE MAGNETOHYDRODYNAMIC ALGORITHMS AND TESTS

JAMES M. STONE[1] AND MICHAEL L. NORMAN[1]
National Center for Supercomputing Applications, 5600 Beckman Institute, Drawer 25, University of Illinois at Urbana-Champaign,
405 North Mathews Avenue, Urbana, IL 61801

ABSTRACT

In this, the second of a series of three papers, we continue a detailed description of ZEUS-2D, a numerical code for the simulation of fluid dynamical flows in astrophysics including a self-consistent treatment of the effects of magnetic fields and radiation transfer. In this paper, we give a detailed description of the magnetohydrodynamical (MHD) algorithms in ZEUS-2D.

The recently developed constrained transport (CT) algorithm is implemented for the numerical evolution of the components of the magnetic field for MHD simulations. This formalism guarantees the numerically evolved field components will satisfy the divergence-free constraint at all times. We find, however, that the method used to compute the electromotive forces must be chosen carefully to propagate accurately all modes of MHD wave families (in particular shear Alfvén waves). A new method of computing the electromotive force is developed using the method of characteristics (MOC). It is demonstrated through the results of an extensive series of MHD test problems that the resulting hybrid MOC-CT method provides for the accurate evolution of all modes of MHD wave families.

Subject headings: hydrodynamics — methods: numerical — MHD — radiative transfer

1. INTRODUCTION

Magnetic fields can play a crucial role in the dynamics of many astrophysical systems. Magnetohydrodynamical (MHD) processes have been identified as important to the understanding of the tenuous solar corona, the interstellar medium and star forming regions, protostellar mass outflows and jets, accretion flows onto magnetic white dwarfs and neutron stars, and extragalactic radio sources. It is vital that theoretical modeling of these systems be able to account for MHD effects in a self-consistent fashion. For this reason, we have developed a general purpose fluid dynamics code, called ZEUS-2D, for modeling astrophysical systems including a self-consistent treatment of the effects of magnetic fields and radiation transfer. In a previous paper (Stone & Norman 1992, hereafter Paper I), we described the hydrodynamic (HD) algorithms in ZEUS-2D. In this paper, we describe the algorithms implemented in ZEUS-2D for the self-consistent evolution of magnetic fields which, when coupled to the HD algorithms described in Paper I, allow for MHD simulations. In a subsequent paper (Stone, Mihalas, & Norman 1992, hereafter Paper III) we describe the two-dimensional radiation transport module implemented in ZEUS-2D to allow for radiation hydrodynamical (RHD) simulations.

The algorithms for evolving the magnetic field presented in this paper are self-contained and independent of the HD algorithms used. It would be possible to implement these algorithms in almost any explicit Eulerian hydrocode based on the method of finite-differences. The method could also be

adapted to Lagrangean or time implicit codes with some modifications. The level of discussion in this paper will be comprehensive enough to allow others to implement and/or modify the method. We also present detailed results from an extensive series of test problems we have performed on our algorithms, which will be useful for comparisons to other schemes. We do not present the results of specific applications of ZEUS-2D to astrophysical problems here: such calculations are presented elsewhere (Stone 1990).

The organization of this paper is as follows. We begin the discussion in § 2 with the equations of MHD which must be solved by ZEUS-2D. In § 3, we give a detailed description of the algorithms implemented for evolving the magnetic fields, and how these algorithms are incorporated into the rest of the ZEUS-2D code. In § 4 we describe the results of the test problems we have performed, while in § 5 we summarize.

2. THE EQUATIONS OF MAGNETOHYDRODYNAMICS

The dynamics of a plasma which is threaded by a large-scale magnetic field is influenced by the magnetic stresses exerted on moving, charged particles. In turn, the motion of the charged particles can influence the strength and distribution of the magnetic field. At the microscopic level (where particle gyroradii are of the same order as the scale of interest), the evolution of the plasma is given by the Maxwell-Boltzmann equations which describe the evolution of the particle distribution function. At a macroscopic level (where particle gyroradii are much smaller than the scale of interest), one can use a simpler, statistical description of the system by evolving the macroscopic conserved quantities with the equations of ideal MHD. Much like the equations of HD, these equations are derived by

---

[1] Also Department of Astronomy, University of Illinois at Urbana-Champaign.

taking velocity moments of the Maxwell-Boltzmann equations assuming quasi-neutrality and an Ohm's Law closure for the current density (see, e.g., Spitzer 1962). With these assumptions, we can write the MHD equations as (Jackson 1975)

$$\frac{D\rho}{Dt} + \rho \nabla \cdot \boldsymbol{v} = 0 \; , \qquad (1)$$

$$\rho \frac{D\boldsymbol{v}}{Dt} = -\nabla p - p\nabla\Phi + \frac{1}{4\pi}(\nabla \times \boldsymbol{B}) \times \boldsymbol{B} \; , \qquad (2)$$

$$\rho \frac{D}{Dt}\left(\frac{e}{\rho}\right) = -p\nabla \cdot \boldsymbol{v} \; , \qquad (3)$$

$$\frac{\partial \boldsymbol{B}}{\partial t} = \nabla \times (\boldsymbol{v} \times \boldsymbol{B}) \; , \qquad (4)$$

where the system of equations is closed with a given equation of state $p = p(\rho, e)$ and the Poisson equation which determines the gravitational potential Φ. In choosing the specific form of the terms involving the magnetic field $\boldsymbol{B}$ in equations (2) and (4), we have made several additional assumptions. For instance, the Lorentz force term $\boldsymbol{j} \times \boldsymbol{B}$ added to the equation of motion (2) ignores the displacement current in Ampere's Law, which is valid only for low-frequency phenomena, such as are of interest here. In Faraday's Law (eq. [4]) we have eliminated the electric field by keeping only the advection term in the generalized Ohm's Law. This is justified because astrophysical resistivities are generally so low that the magnetic field is effectively "frozen-in" to the bulk of the fluid. For many astrophysical systems the degree of ionization of the gas is quite high, therefore collisions between neutral and charged particles are frequent enough to maintain a tight coupling between the two, and the flux-freezing approximation is accurate. However, in some systems (for example, the densest parts of molecular clouds) the degree of ionization of the gas can drop substantially. In this case, collisions are not frequent enough to maintain perfect coupling, and the plasma (and magnetic field) can drift relative to the neutral gas, a process known as *ambipolar diffusion*. In this work, we do not account for the effects of ambipolar diffusion or resistivity. However, incorporating the appropriate diffusion terms into our current algorithms is straightforward, and would be a fruitful direction for future work.

Like the HD equations, the MHD equations are a coupled set of nonlinear hyperbolic PDEs. We have already described many of the necessary numerical algorithms for generating solutions to these equations in Paper I. In the next section, we describe the additions and modifications to the algorithms we have implemented in the ZEUS-2D code to evolve the magnetic field components.

3. THE MHD ALGORITHMS IN ZEUS-2D

There are two principal difficulties associated with the numerical solution of the MHD equations as compared to the HD equations. The first difficulty is that Maxwell's equations require the magnetic field satisfy the divergence-free constraint ($\nabla \cdot \boldsymbol{B} = 0$) at all times. Unless this constraint is built into the

numerical evolution equations, the numerical errors associated with evolving the field components will, in general, not satisfy the divergence-free constraint. Accumulation of these errors can ultimately lead to gross violation of the constraint equation, and this will force termination of the calculation. The reader is referred to Evans & Hawley (1988, hereafter EH) for an informative discussion of this issue; we summarize some of the important points below. The second difficulty is that MHD flows possess entirely new families of wave modes in comparison to HD flows. This not only results in a wealth of new physical effects, but also has implications for the numerical algorithms. One must ensure that the numerical algorithms provide for the stable and accurate propagation of all possible MHD waves.

In order to circumvent the first difficulty, the need to develop algorithms which evolve divergence-free fields has long been recognized. Until recently, the traditional approach has been to evolve the magnetic vector potential (defined via $\boldsymbol{B} = \nabla \times \boldsymbol{A}$) rather than the field components themselves. One then derives the field components from numerical derivatives of the vector potential whenever needed. Provided that the finite-difference representations of the divergence and curl operators are constructed properly, the discrete representation of the vector identity $\nabla \cdot \nabla \times \boldsymbol{A} = 0$ will be satisfied exactly. In two dimensions, the evolution equations for the vector potential reduce to an advection equation for a single scalar. This approach was the method implemented in the original ZEUS code for MHD simulations of axisymmetric jets (Clarke 1988).

The difficulty with evolving the vector potential rather than the field components themselves is constructing an accurate representation of the Lorentz force $(4\pi)^{-1}(\nabla \times \boldsymbol{B}) \times \boldsymbol{B}$ which requires taking a second derivative of the vector potential. Clarke, Norman, & Burns (1989) have argued that in order to achieve a first-order accurate representation of the Lorentz forces, a third-order accurate scheme must be used for evolving the vector potential (such as PPA). However, Choptuik (1986) has emphasized that for smooth functions, taking numerical derivatives does not necessarily reduce the order of accuracy of the derivatives as compared to the corresponding analytic derivative. Nonetheless, Clarke (1988) has demonstrated unequivocally by means of numerical tests that in order to achieve accurate representations of the current (first derivative of the field) in many advection problems, a higher order scheme must be used. Even then, one encounters serious problems due to anomalous current (and force) reversals in the vicinity of sharp features in the magnetic field such as shocks and contact discontinuities. Such force reversals will couple directly to the dynamics of the flow, and will produce spurious accelerations and heating. Recently, EH have developed the constrained transport (CT) method which incorporates the divergence-free constraint directly into the finite-differenced form of the magnetic field evolution equations. Since the field components themselves are evolved, accurate and smooth representations of the current can be achieved without anomalous reversals (since numerical second derivatives are not needed), while the method also guarantees that the constraint equation $\nabla \cdot \boldsymbol{B} = 0$ will be satisfied to machine roundoff at all times. For these reasons, we have chosen to implement the CT scheme in ZEUS-2D.

In addition to ensuring the algorithm can evolve divergence free fields, we must also address the second difficulty posed by the numerical solution of the MHD equations, namely developing a scheme which gives an accurate representation of all MHD wave modes. One might assume that the same types of upwind schemes used to evolve the HD variables might be adopted to evolve the magnetic field components as well. However, MHD flows possess a family of incompressible transverse wave modes, called Alfvén waves, which tightly couple the evolution of the velocity and magnetic field components. HD flows possess no analog to the Alfvén wave family. We have found that if the same upwind schemes used to evolve the HD variables are applied to the evolution of the MHD equations, the resulting method has a large dispersion error for these waves. This error is particularly evident in the evolution of sharp, discontinuous features, or when smooth features interact with a boundary. In such cases, the dispersion error creates large-amplitude, short-wavelength oscillations which are stable, but are neither damped nor diffused away. The only suitable methods we have found which eliminates this error are schemes which are upwind in the Alfvén wave characteristics (the error can also be eliminated by schemes with a large intrinsic diffusion, however we consider this an unsuitable solution). One suitable method to achieve this is the method of characteristics (MOC). While MHD codes based entirely on the MOC have been developed (Lou, Rosner, & Ulmschneider 1987) and are therefore automatically upwind in all MHD wave families, they sacrifice conservative form and the divergence-free constraint, as well as the simplicity of finite-difference representations of the primitive MHD equations. Thus, as described below, we do not solve the full MHD equations with the MOC, but only the subset which describe the propagation of Alfvén waves as an intermediate step to compute time advanced quantities for the evolution of the field components themselves. In two-dimensional axisymmetric calculations, the toroidal component of the magnetic field is divergence free due to the assumed symmetry, i.e., $\partial B_\phi / \partial \phi \equiv 0$, thus only the poloidal components need be evolved with a constraint preserving formalism such as CT. (Hereafter, we identify the poloidal components of the field as those that lie in the plane of the two-dimensional mesh, while the toroidal component is orthogonal to the mesh). Thus, to evolve the toroidal field, we use a straightforward algorithm based on the MOC, as described in § 3.3, while to evolve the poloidal field component we implement a form of the MOC within the CT formalism, a technique which we refer to as MOC-CT.

We describe in detail the MHD algorithms implemented in ZEUS-2D in the following subsections. We begin in § 3.1 with the centering of the MHD variables. In § 3.2, we describe the evolution of the poloidal field components using the new MOC-CT scheme. Finally, in § 3.3 we describe the MOC scheme for the evolution of the toroidal field components.

3.1. Centering of Variables

Before writing down the finite-difference equations used to evolve the magnetic field, we must first decide on the spatial centering of these variables on the staggered mesh. (The two-dimensional mesh used in the ZEUS-2D code is described in § 4.1 in Paper I, we merely note here the mesh is labeled by the coordinate vectors x_1 and x_2, with the 3-direction taken to be orthogonal to the computational plane.) The correct centering of the magnetic field components is a key aspect of any numerical scheme. Since Alfvén waves couple the components of velocity and magnetic field which are perpendicular to the direction of propagation (e.g., v_1 and B_1 are coupled for waves propagating in the 2-direction, and vice versa), it is natural to center the magnetic components identically to the velocity components. Thus, the 1-component of the magnetic field is face centered in the 1-direction, the 2-component is face centered in the 2-direction, and the 3-component is zone centered (see Fig. 1). With this centering, the poloidal field components are normal to the faces of a control volume defined at zone centers (as is used for the momenta). This centering is different than that originally described in EH. The transformation from the continuum variables in the differential equations to the discrete variables used in the finite-difference equations is then

$$B_1(x_1, x_2) \rightarrow B1(x1a_i, x2b_j) = B1_{i,j},$$

$$B_2(x_1, x_2) \rightarrow B2(x1b_i, x2a_j) = B2_{i,j},$$

$$B_3(x_1, x_2) \rightarrow B3(x1b_i, x2b_j) = B3_{i,j}.$$

An important derived quantity in the MHD equations is the electric current density vector $j = \nabla \times B$. With the above centering of the magnetic field components, the poloidal components of the current density are naturally centered at the positions of the orthogonal components of the magnetic field (so that j_1 is centered at the same position as B_2, j_2 at the position of B_1), while j_3 is centered at zone corners (see Fig. 1).

3.2. Evolving the Poloidal Field

In this section, we describe the algorithms for evolving the poloidal components of the magnetic field implemented in the
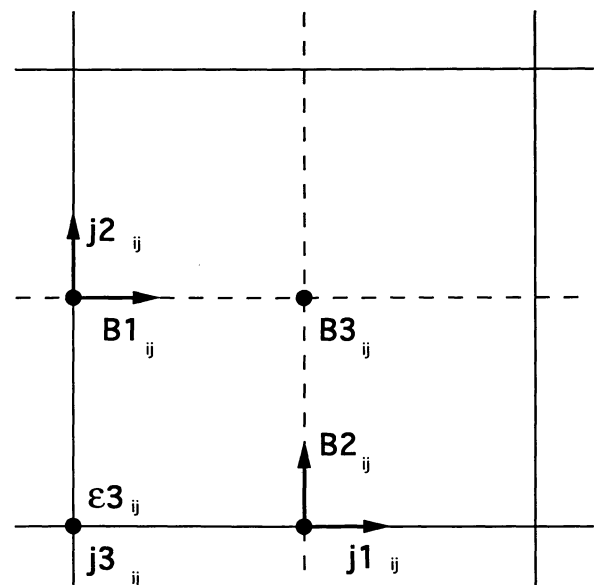

FIG. 1.—Centering of the magnetic field components (B_1, B_2, and B_3) current density components (j_1, j_2, and j_3), and the 3-component of the EMF used in the two-dimensional CT scheme implemented in the ZEUS-2D code.

ZEUS-2D code by focusing on three issues. In § 3.2.1 we summarize the constraint preserving CT formalism, in § 3.2.2 we describe our new MOC-CT scheme which evolves all poloidal MHD wave families accurately, and in § 3.2.3 we describe how the Lorentz force terms are differenced in the momentum equation.

3.2.1. *The CT Scheme*

The fundamental concept of the CT scheme developed by EH is the realization that the constraint equation is satisfied identically by a numerical scheme which evolves the magnetic flux in a conservative fashion. To achieve this, the differential form of Faraday's Law (eq. [4]) can be rewritten using Stoke's theorem in integral form,

$$\frac{\partial \Phi_S}{\partial t} = \oint_{\partial S} (v \times B) \cdot dl, \tag{5}$$

where Φ_S is the magnetic flux piercing a surface S bounded by ∂S. Physically, equation (5) states that the rate of change of the flux through a surface S is given by the path integral of the electromotive force (EMF, defined via $\epsilon = v \times B$) around the edges of that surface. With the centering of the magnetic field components used in ZEUS-2D (described in § 3.1), the components of the flux are centered at the faces of a control volume. We can develop a finite difference representation of equation (5) for the flux components as follows. The area of each interface of the control volume is bounded by a closed contour along each of its four edges. We center the components of the EMF at the center of each edge, so that when projected onto the two-dimensional grid, $\epsilon_1 = v_2 B_3 - v_3 B_2$ is face centered in the 2-direction (i.e., at the same position as B_2), $\epsilon_2 = v_3 B_1 - v_1 B_3$ is face centered in the 1-direction (i.e., at the same position as B_1), and $\epsilon_3 = v_1 B_2 - v_2 B_1$ is located at zone corners (see Fig. 2). Then, assuming the components of the EMF are constant along all edges, we can construct finite-difference approximations to the components of equation (5) using the right-handed rule

$$(\Phi 1_{i,j}^{n+1} - \Phi 1_{i,j}^n)/\Delta t = -\epsilon 2_{i,j} \Delta x2 - \epsilon 3_{i,j} \Delta x3$$
$$+ \epsilon 2_{i,j} \Delta x2 + \epsilon 3_{i,j+1} \Delta x3$$
$$= +(\epsilon 3_{i,j+1} - \epsilon 3_{i,j}) \Delta x3, \tag{6}$$

$$(\Phi 2_{i,j}^{n+1} - \Phi 2_{i,j}^n)/\Delta t = +\epsilon 1_{i,j} \Delta x1 - \epsilon 3_{i+1,j} \Delta x3$$
$$- \epsilon 1_{i,j} \Delta x1 + \epsilon 3_{i,j} \Delta x3$$
$$= -(\epsilon 3_{i+1,j} - \epsilon 3_{i,j}) \Delta x3. \tag{7}$$

The arrows in Figure 2 denote the correct direction for the contour integration resulting in equations (6) and (7). Note that for two-dimensional calculations, the 1- and 2-components of the EMF cancel from the evolution equations by symmetry.

By adding equations (6) and (7) together, we can calculate the new total flux through the surfaces of the control volume. Since the contribution from the EMF along each edge appears once in each equation with opposite signs, all EMF terms will cancel in the full sum for the total flux. Thus, we see that if the
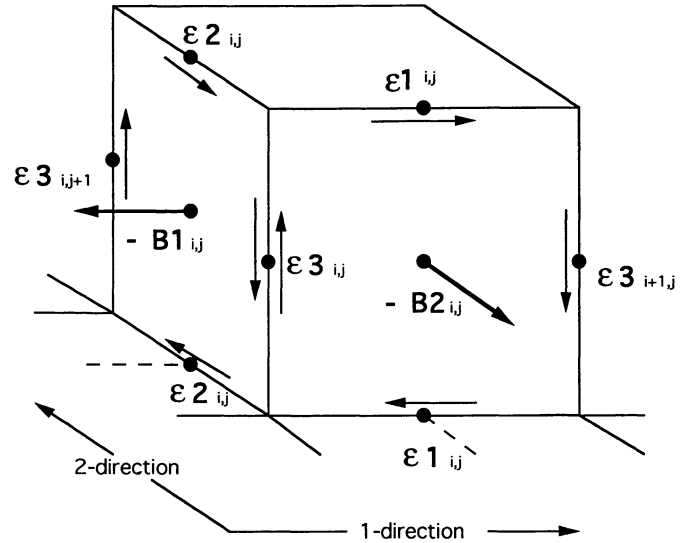

FIG. 2.—When the two-dimensional grid is expanded in the 3-direction (plotted vertically in this figure), the closed contours around which the EMF is integrated to evolve the magnetic field components become evident. Arrows indicate the direction of the path integral around the edges. Note the magnetic field components are shown pointing in the opposite direction of the coordinate unit vectors.

old flux obeyed the constraint equation (i.e., $\int_S \Phi \cdot dS = 0$ by Gauss' Law) then the new flux will continue to do so. In other words, the evolution equations (6) and (7) guarantee that changes in the flux obey the divergence-free constraint. Numerically, we can achieve global conservation by computing the EMF over the whole grid once and for all, and using the same values to update neighboring cells. Then, if one computes the total flux piercing the computational domain by summing the evolution equations (6) and (7) over all zones, we will achieve conservation of flux to machine round-off error. As pointed out by EH, this is exactly analogous to the more familiar conservative differencing schemes for the HD variables (such as mass density), whereby one solves the integral form of the advection equations using fluxes computed through each zone interface, and then uses that flux twice, once when mass leaves a zone and once when it enters the adjacent zone.

By substituting expressions for the magnetic fluxes in terms of the control volume surface areas and magnetic field components, we can rewrite equations (6) and (7) as evolution equations for the field components themselves. Since EH were motivated by general relativistic MHD simulations, they derived covariant expressions for the evolution equations using the magnetic vector density. These equations contain no reference to the metric tensor describing the particular coordinate system being used, and are therefore valid in arbitrary coordinate systems. In this work, however, we will only be interested in nonrelativistic MHD for which the components of the metric tensor are known analytically. It is therefore more convenient for us to use covariant evolution equations in which the components of the metric tensor appear explicitly, rather than transforming the variables to use the magnetic vector density. Using the coordinate independent differencing formalism described

in Paper I, covariant expressions for the flux components and control volume edge lengths are

$$\Phi_1 = h_2 h_3\, dx_2\, dx_3\, B_1 , \tag{8}$$

$$\Phi_2 = h_1 h_3\, dx_1\, dx_3\, B_2 , \tag{9}$$

$$\Delta x3 = h_3\, dx_3 . \tag{10}$$

Substituting these expressions into equation (6) and (7) and differencing yields

$$B1_{i,j}^{n+1} = [B1_{i,j}^n\, g2a_i^n\, g31a_i^n\, g32b_j^n\, dx2a_i^n$$
$$+ \Delta t(g31a_i^{n+1/2}\, g32a_{j+1}^{n+1/2}\, \epsilon3_{i,j+1}^{n+1/2}$$
$$- g31a_i^{n+1/2}\, g32a_j^{n+1/2}\, \epsilon3_{i,j}^{n+1/2})]/$$
$$g2a_i^{n+1}\, g31a_i^{n+1}\, g32b_j^{n+1}\, dx2a_j^{n+1} , \tag{11}$$

$$B2_{i,j}^{n+1} = [B2_{i,j}^n\, g31b_i^n\, g32a_j^n\, dx1a_i^n$$
$$- \Delta t(g31a_{i+1}^{n+1/2}\, g32a_j^{n+1/2}\, \epsilon3_{i+1,j}^{n+1/2}$$
$$- g31a_i^{n+1/2}\, g32a_j^{n+1/2}\, \epsilon3_{i,j}^{n+1/2})]/$$
$$g31b_i^{n+1}\, g32a_j^{n+1}\, dx1a_i^{n+1} . \tag{12}$$

By using the metric scale factor variables g_2, g_{31}, and g_{32} (eqs. [15]–[20] in Paper I) we have conformed to the covariant differencing formalism described in § 4.2 of Paper I. Note the use of the metric scale factor variables at both the old and the new time levels to account for compression and expansion of the grid (if it is moving), and that the terms involving the EMF are time centered (measured at $n + 1/2$). Equations (11) and (12) are the finite-difference expressions solved in ZEUS-2D to evolve the poloidal field components, all that remains to be specified are the EMFs.

One final comment regarding the CT scheme as a whole is that it guarantees that an *initially* divergence-free field will remain divergence free during evolution. However, one must take care that the initial field is in fact divergence-free! In practice, we find that using the vector potential to initialize a field configuration (as suggested by EH) is a convenient way of achieving this. Perhaps more importantly, one must also ensure that the boundary conditions applied to the field components do not introduce divergence into the computational domain, a point also emphasized by EH. In this work, this is achieved by applying boundary conditions to the EMF, and *evolving* the field components in the ghost zones. The various types of boundary conditions which can be applied to the EMFs are given in § 3.4.

3.2.2. Computing the EMF

In principle, one could use *any* method to compute the EMF within the CT formalism and still maintain divergence-free fields. In practice, however, a method must be used which satisfies numerical stability requirements, and gives an accurate description of the MHD flow. The stability requirements arise because of the mathematical nature of the transport operators in the induction equation which give rise to an EMF due to fluid advection. EH described a stable method for comput-

ing the EMF for advection problems. Schematically, the method can be written as

$$\epsilon3_{i,j}^{n+1/2} = v1_{i,j}^{*,n+1/2} B2_{i,j}^{*,n+1/2} - v2_{i,j}^{*,n+1/2} B1_{i,j}^{*,n+1/2} , \tag{13}$$

where $v_{i,j}^{*,n+1/2}$ and $B_{i,j}^{*,n+1/2}$ represent time centered values for these variables at the same spatial location on the grid as the EMF (zone corners). Note that some sort of space and time interpolation is needed to compute the time-centered components of the velocity and magnetic field at zone corners from the face centered values evolved in ZEUS-2D. EH used simple arithmetic averaging of the velocity at the old time level to compute the components of $v_{i,j}^{*,n+1/2}$ (i.e., the velocity is not time-centered), and upstream interpolation using the van Leer algorithm described in Paper I to compute the components of $B_{i,j}^{*,n+1/2}$. Although this formulation for computing the EMF was found to be entirely adequate the advection test problems given in EH, we have found that when used for fully dynamical problems, it is unable to propagate shear Alfvén waves along poloidal field lines accurately, as will be demonstrated by the results of some of our test problems (see § 4.6). As mentioned previously, this has motivated the development of our MOC-CT scheme described here.

The fundamental component of the MOC-CT scheme is to use the MOC to compute time advanced values for *both* the velocity and magnetic field components in order to compute the EMF. An important simplification of this MOC step is that only the Alfvén wave characteristics are used to compute the time-advanced values; the compressive (fast and slow) MHD wave characteristics are excluded. This simplification results from the fact that the compressive wave families are tightly coupled thermodynamically to the HD. Thus, the numerical algorithms used to evolve the HD (which is used to evolve the compressive HD [sound] waves) will also evolve the compressive MHD waves accurately, so that the full MHD algorithm in ZEUS-2D can account for all MHD wave families present in multidimensional flows. This point will be demonstrated through an extensive series of test problems presented in § 4.

The MOC differential equations used to compute the time advanced values of the velocity and magnetic field needed for the EMF (i.e., $v^{*,n+1/2}$ and $B^{*,n+1/2}$) can be easily derived by considering the MHD equations for a one-dimensional, moving, *incompressible* fluid. With these restrictions, the full set of MHD equations reduce simply to

$$\frac{\partial v}{\partial t} = \frac{B_x}{\rho} \frac{\partial B}{\partial x} - \frac{\partial}{\partial x}(v_x v) , \tag{14}$$

$$\frac{\partial B}{\partial t} = B_x \frac{\partial v}{\partial x} - \frac{\partial}{\partial x}(v_x B) , \tag{15}$$

where all variables are a function of x only, we choose the units of B such that $\mu_0 = 1$, and we denote the components of velocity and magnetic field in the x-direction by v_x and B_x, respectively. Note that the divergence-free constraint in one dimension (which implies $\partial B_x/\partial x \equiv 0$) and the incompressibility condition in one dimension (which implies $\partial v_x/\partial x \equiv 0$) has allowed us to simplify the induction equation (15) and the Lorentz force terms in the equation of motion (14) consider-

ably. It is straightforward to show that the coupling in the leading terms in equations (14) and (15) describe pure (transverse) Alfvén waves propagating in the x-direction, while the second terms in these equations accounts for fluid advection. Thus, these equations only describe the propagation of information in a moving fluid via Alfvén waves and do not admit any compressive wave modes. We can rewrite the coupled equations (14) and (15) in characteristic form by multiplying equation (15) by $\rho^{-1/2}$ and then adding and subtracting them, yielding

$$\frac{Dv}{Dt} \mp \frac{1}{\rho^{1/2}} \frac{DB}{Dt} = 0 . \tag{16}$$

The minus sign denotes the characteristic equation along the forward facing characteristic C^+, while the plus sign denotes the characteristic equation along the backward facing characteristic C^-. The comoving derivative used in equation (16) is defined as

$$D/Dt = \partial/\partial t + (v_x \pm B_x/\rho^{1/2})\partial/\partial x , \tag{17}$$

where the plus (minus) sign is taken for the comoving derivative along the C^+ (C^-) characteristic. Note that the coefficient of the second term in the comoving derivative is just the Alfvén velocity in the moving fluid, $v_x \pm v_A$. Physically, equations (16) and (17) state that along characteristics, which are straight lines in spacetime with slopes of $v_x \pm v_A$, the changes in the velocity and magnetic field components in each direction are not independent.

The finite-difference equations used to solve the characteristic equations (16) and (17) can be generated as follows. Consider the one-dimensional spacetime diagram centered at the positions of the EMF, where we require the partially updated values $v_i^{*,n+1/2}$ and $B_i^{*,n+1/2}$ (see Fig. 3). Note that by construction, the partially advanced quantities are centered in space between the currently known velocities and magnetic field at time level n. On our two-dimensional, staggered mesh this implies the $v_i^{*,n+1/2}$ and $B_i^{*,n+1/2}$ are located at cell corners, the same as the EMF (see Fig. 1). Extrapolating back in time along the characteristics C^+ and C^- to time level n, where values for all variables are known, defines the "footpoints." By using upwind interpolation at time level n (e.g., donor cell, van Leer or PPA), we can compute the time-averaged values for these variables in each domain of dependence, i.e., $v_i^{-,n}$ and $B_i^{-,n}$ on the C^- characteristic, and $v_i^{+,n}$ and $B_i^{+,n}$ on the C^+ characteristic. For both the velocities and the magnetic fields the characteristic speed $v_x \pm v_A$ are used to compute upwind values. Given values for the variables at the footpoints, we difference the characteristic equations along C^+ or C^- as

$$(v_i^{*,n+1/2} - v_i^{+,n}) - (B_i^{*,n+1/2} - B_i^{+,n})/(\rho_i^+)^{1/2} = 0 , \tag{18}$$

$$(v_i^{*,n+1/2} - v_i^{-,n}) + (B_i^{*,n+1/2} - B_i^{-,n})/(\rho_i^-)^{1/2} = 0 . \tag{19}$$

In order to approximately time center the denominator of the second term in each of these equations, we set $\rho_i^+ = \rho_{i-1}^n$ and $\rho_i^- = \rho_i^n$. These two linear equations for the two unknowns $v_i^{*,n+1/2}$ and $B_i^{*,n+1/2}$ are then solved directly.

For our multidimensional calculations, we solve the characteristic equations in a directionally split fashion in order to
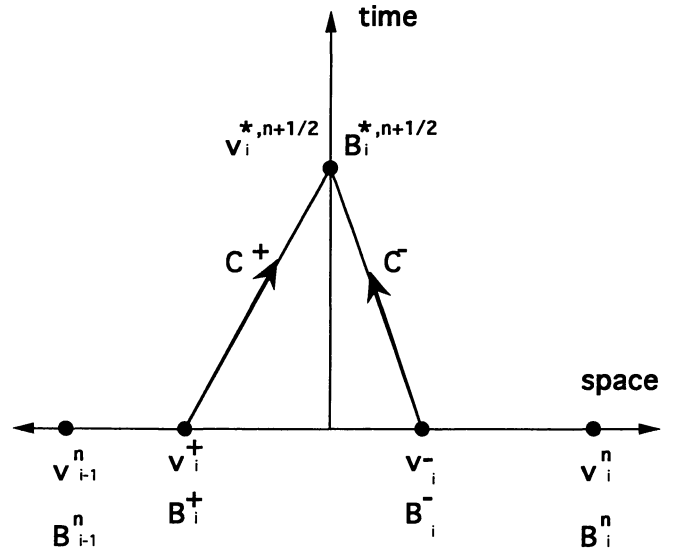
FIG. 3.—One-dimensional spacetime diagram showing the locations of the forward and backward facing characteristics C^+ and C^-, which are used to compute the partially advanced quantities v^* and B^* with the method of characteristics. In space v^* and B^* are centered at zone interfaces, in time they are the half-time step $n + 1/2$. The time-averaged values for the variables over the domain of dependence for each footpoint of the characteristics are computed using upwind interpolation between quantities at time level n, located at zone centers.

construct time-advanced values for all of the components of velocity and magnetic field ($v^{*,n+1/2}$ and $B^{*,n+1/2}$). We proceed by solving at every grid point the pair of characteristic equations which represent the propagation of Alfvén waves in the 2-direction, namely

$$\frac{Dv_1}{Dt} \mp \frac{1}{\rho^{1/2}} \frac{DB_1}{Dt} = 0 , \tag{20}$$

where

$$D/Dt = \partial/\partial t + (v_2 \pm B_2/\rho^{1/2})/h_2\partial/\partial x_2 . \tag{21}$$

Equation (20) is differenced in the manner of equations (18)–(19), except the characteristic speeds in the 2-direction used to upwind the variables at the footpoints are $v_2 \pm B_2/\rho^{1/2}$. The solution of these difference equations then yields $v1_{i,j}^{*,n+1/2}$ and $B1_{i,j}^{*,n+1/2}$ at every cell corner. We then solve, at every grid point, a similar pair of characteristic equations which represent the propagation of Alfvén waves in the 1-direction, namely

$$\frac{Dv_2}{Dt} \mp \frac{1}{\rho^{1/2}} \frac{DB_2}{Dt} = 0 , \tag{22}$$

where

$$D/Dt = \partial/\partial t + (v_1 \pm B_1/\rho^{1/2})\partial/\partial x_1 . \tag{23}$$

Equation (22) is again differenced in the manner of equations (18)–(19), except the characteristic speeds in the 1-direction used to upwind the variables at the footpoints are $v_1 \pm B_1/\rho^{1/2}$.

The solution of these difference equations then yields $v2_{i,j}^{*,n+1/2}$ and $B2_{i,j}^{*,n+1/2}$ at every cell corner. Note that, due to the centering of the velocity and magnetic field components at the same position on the mesh, we can naturally apply the MOC to the coupled pairs in each direction, and the resulting updated values will be known at cell corners in both cases. In fact, it is for this reason that we chose a different centering than originally described in EH. We have found that, for grids in which the velocity and magnetic field components are not cospatial, averaging of one to the position of the other interferes with the tracking of Alfvén waves with the characteristic method, and does not produce a suitable algorithm.

Once both components of the variables at the advanced time is known at every cell corner, we use them to compute the EMF via equation (13) and proceed with the CT update. Note that this direction-splitting of the scheme can be naturally extended to three-dimensional calculations (Clarke, Stone, & Norman 1990). Of course, directionally splitting the equations in this fashion is only an approximation to the true characteristics problem in multidimensions. A more accurate result would probably be achieved by interpolating along the principle axes of the characteristic cone in multidimensions, rather than along the components along coordinate grid lines as we have done here. One problem with implementing the former method on a staggered mesh is that the precise direction of the magnetic field lines (and thus characteristic) is not known at a specific position in space. Averaging of field components to the same position to compute the direction of the field there will probably introduce diffusion into the result, much in the same way that our current directional splitting is likely to do. Which formalism is the most accurate is a subject for future numerical investigations. To demonstrate the accuracy of our present formulation, we present the results of an extensive series of test problems in § 4.

3.2.3. *Differencing the Lorentz Force Terms*

For the accurate evolution of the Alfvén waves it is not sufficient to use only the MOC to compute partially updated variables $v^{*,n+1/2}$ and $B^{*,n+1/2}$ for the EMF and then update the magnetic field components using CT. We must also update the Lorentz force term in the equations of motion (2) using partially updated values of the magnetic field resulting from an MOC calculation similar to that used in computing the EMF.

Expanding the vector operators in the equation of motion (2), we can write the Lorentz force terms as

$$\frac{\partial v_1}{\partial t} = \frac{B_2}{\rho h_2}\frac{\partial B_1}{\partial x_2} - \frac{B_2}{\rho h_2}\frac{\partial}{\partial x_1}(h_2 B_2) - \frac{B_3}{\rho h_3}\frac{\partial}{\partial x_1}(h_3 B_3), \quad (24)$$

$$\frac{\partial v_2}{\partial t} = \frac{B_1}{\rho h_2}\frac{\partial}{\partial x_1}(h_2 B_2) - \frac{B_1}{\rho h_2}\frac{\partial B_1}{\partial x_2} - \frac{B_3}{\rho h_2 h_3}\frac{\partial}{\partial x_2}(h_3 B_3). \quad (25)$$

We identify the first term in these equations as those which, when coupled to the appropriate components of the induction equation, describe the propagation of Alfvén waves, while the latter terms represent changes in momentum due to gradients of magnetic pressure. We can split the update for the Lorentz force into two parts. The first partial update is performed in the source step using the finite-difference equations

$$\frac{v1_{i,j}^{n+a} - v1_{i,j}^n}{\Delta t} = -\frac{\langle B2_{i,j}\rangle}{(d_{i-1,j} + d_{i,j})}$$

$$\times \left[\frac{g2b_i(B2_{i,j} + B2_{i,j+1}) - g2b_{i-1}(B2_{i-1,j} + B2_{i-1,j+1})}{g2a_i dx1b_i}\right]$$

$$- \frac{(B3_{i-1,j} + B3_{i,j})}{(d_{i-1,j} + d_{i,j})}\left(\frac{g31b_i B3_{i,j} - g31b_{i-1} B3_{i-1,j}}{g31a_i dx1b_i}\right), \quad (26)$$

$$\frac{v2_{i,j}^{n+a} - v2_{i,j}^n}{\Delta t} = -\frac{\langle B1_{i,j}\rangle}{(d_{i-1,j} + d_{i,j})}$$

$$\times \left(\frac{(B1_{i,j} + B1_{i+1,j}) - (B1_{i,j-1} + B1_{i+1,j-1})}{g2b_i dx2b_j}\right)$$

$$- \frac{(B3_{i,j-1} + B3_{i,j})}{(d_{i,j-1} + d_{i,j})}\left(\frac{g32b_j B3_{i,j} - g32b_{j-1} B3_{i,j-1}}{g2b_i g32a_j dx2b_j}\right), \quad (27)$$

$$\langle B1_{i,j}\rangle = (B1_{i,j} + B1_{i+1,j} + B1_{i,j-1} + B1_{i+1,j-1})/4, \quad (28)$$

$$\langle B2_{i,j}\rangle = (B2_{i,j} + B2_{i,j+1} + B2_{i-1,j} + B2_{i-1,j+1})/4. \quad (29)$$

These terms, which account for gradients of magnetic pressure, are added in "Substep 1" of the source step. (We refer the reader to § 4.3 of Paper I for a description of the "source step" in the ZEUS-2D code). Note these terms do not use time advanced values of the magnetic field components, but like the rest of the source step use only the currently stored values of variables on the right-hand side.

The second partial update for the Lorentz force terms that result in Alfvén wave motion is added when the MOC-CT evolution is performed. The finite-difference equations for this update utilize the time advanced variables $B1_{i,j}^{',n+1/2}$ and $B2_{i,j}^{',n+1/2}$ computed from a MOC solution of the directionally split characteristic equations in a frame *comoving* with the fluid, so that

$$\frac{v1_{i,j}^{n+1} - v1_{i,j}^{n+a}}{\Delta t} = \frac{2\langle B2_{i,j}\rangle}{(d_{i-1,j} + d_{i,j}}\left(\frac{B1_{i,j+1}^{',n+1/2} - B1_{i,j}^{',n+1/2}}{g2a_i dx2a_j}\right), \quad (30)$$

$$\frac{v2_{i,j}^{n+1} - v2_{i,j}^{n+a}}{\Delta t} = \frac{2\langle B1_{i,j}\rangle}{(d_{i-1,j} + d_{i,j})}$$

$$\times \left(\frac{g2a_{i+1} B2_{i+1,j}^{',n+1/2} - g2a_i B2_{i,j}^{',n+1/2}}{g2b_i dx1a_i}\right). \quad (31)$$

Note that the time advanced values $B1_i^{',n+1/2}$ and $B2_i^{',n+1/2}$ used here are *not* the same as those used to compute the EMF. The reason for this difference is related to the fact that the CT formalism is not an operator split scheme. Thus, the coupled momentum and induction equations used to generate the characteristic equations (i.e., eqs. [14]–[15]) in the MOC-CT scheme describe the propagation of Alfvén waves in an *Eulerian* frame of reference. However, since the momentum equation is operator split, the Lorentz force term is effectively applied in a *Lagrangean* frame of reference. Thus, the coupled momentum and induction equations used to generate the characteristic equations for the Lorentz force describe the propagation of Alfvén waves in the comoving frame (i.e., they are identical to eqs. (14)–(15) but the second term on the right-

hand side is dropped). The characteristic equations used to compute $B_1'^{n+1/2}$ and $B_2'^{n+1/2}$ used in equations (30) and (31) are identical to equations (20) and (22), respectively, but now the comoving derivative used in these equations are

$$D/Dt = \partial/\partial t \pm (B_2/\rho^{1/2})/h_2 \partial/\partial x_2 , \quad (32)$$

for Alfvén waves propagating in the 2-direction (eq. [20]), and

$$D/Dt = \partial/\partial t \pm (B_1/\rho^{1/2})\partial/\partial x_1 , \quad (33)$$

for Alfvén waves propagating in the 1-direction (eq. [22]). To compute the $B_1'^{n+1/2}$ and $B_2'^{n+1/2}$ needed in equations (30) and (31), we solve the same finite-difference equations as before (eqs. [18]–[19]) but the variables at the footpoints are up-winded using the characteristic speeds $\pm B_2/\rho^{1/2}$ for waves propagating in the 2-direction and $\pm B_1/\rho^{1/2}$ for waves propagating in the 1-direction. Note that $v_1'^{n+1/2}$ and $v_2'^{n+1/2}$, which also result from solving equations (18) and (19), are not needed here and are discarded.

3.3. Evolving the Toroidal Field

For two-dimensional simulations, the toroidal component of the magnetic field will satisfy the constraint equation at all times by symmetry. Thus, we do not need to use a constraint preserving algorithm such as CT for evolving the toroidal field. However, specialized algorithms are still required to propagate torsional Alfvén waves accurately, as described below. We have achieved self-consistency in our algorithms in that, for stationary flows, the MOC-CT scheme described above reduces to the algorithm used here.

For two-dimensional calculations, the 3-components of the equation of motion and induction equation can be written in full as

$$\frac{\partial v_3}{\partial t} = -\frac{1}{h_2 h_3}\frac{\partial}{\partial x_1}(h_2 h_3^2 v_1 v_3) - \frac{1}{h_2 h_3}\frac{\partial}{\partial x_2}(h_3^2 v_2 v_3)$$
$$+ \frac{B_1}{\rho h_3}\frac{\partial}{\partial x_1}(h_3 B_3) + \frac{B_2}{\rho h_2 h_3}\frac{\partial}{\partial x_2}(h_3 B_3) , \quad (34)$$

$$\frac{\partial B_3}{\partial t} = -\frac{1}{h_2}\frac{\partial}{\partial x_1}(h_2 v_1 B_3) - \frac{1}{h_2}\frac{\partial}{\partial x_2}(v_2 B_3)$$
$$+ B_1 h_3 \frac{\partial}{\partial x_1}(v_3/h_3) + B_2 h_3/h_2 \frac{\partial}{\partial x_2}(v_3/h_3) . \quad (35)$$

The leading two terms in each of these equations are transport terms, accounting for advection of v_3 or B_3 respectively due to fluid motion in each direction, while the other two terms are source terms. Following the operator splitting formalism described in Paper I, we split the update of v_3 and B_3 due to source and transport terms into two separate steps. In the source step, we solve finite-difference approximations to

$$\frac{\partial v_3}{\partial t} = \frac{B_1}{\rho h_3}\frac{\partial}{\partial x_1}(h_3 B_3) + \frac{B_2}{\rho h_2 h_3}\frac{\partial}{\partial x_2}(h_3 B_3) , \quad (36)$$

$$\frac{\partial B_3}{\partial t} = B_1 h_3 \frac{\partial}{\partial x_1}\left(\frac{v_3}{h_3}\right) + \frac{B_2 h_3}{h_2}\frac{\partial}{\partial x_2}\left(\frac{v_3}{h_3}\right) , \quad (37)$$

while in the transport step we use the integral forms of the equations to account for advection

$$\frac{d}{dt}\int_V \rho h_3 v_3 dV = -\int_{dV} \rho h_3 v_3 (v - v_g)\cdot dS , \quad (38)$$

$$\frac{d}{dt}\int_A B_3 dA = -\int_{\partial A} B_3 (v - v_g)\cdot dl . \quad (39)$$

Note that in equation (39) the magnetic field is integrated over the zone area rather than volume, since it is more natural to transport magnetic flux.

The source terms in equations (36)–(37) are responsible for torsional Alfvén wave motion. We have found that straightforward finite-differencing of these source terms does not yield an accurate algorithm for evolving torsional Alfvén waves which contain discontinuities. We have tested many numerical algorithms for evolving equations (36)–(37). Of the algorithms we have tested, we have found that the only suitable ones are those which are either very diffusive (such as Lax-Friedrichs, or Lax-Wendroff), or those which use upwind differencing along the characteristics of the torsional Alfvén waves. Since the latter scheme can provide for a much less diffusive algorithm, we have chosen to implement it in ZEUS-2D. Our formalism is to use the MOC to estimate partially updated values for v_3 and B_3 at the half-time step, which can then be used in finite difference forms of equations (36) and (37) to evolve the variables. We do not use the MOC to actually evolve the variables themselves, but merely as an intermediary step.

The characteristic equations used to compute the partially updated values for v_3 and B_3 can be derived as follows. We begin by rewriting equations (36) and (37) in a more compact form

$$\frac{\partial}{\partial t}\left(\frac{v_3}{h_3}\right) = \left(\frac{1}{h_3}\right)^2\left[\frac{B_1}{\rho}\frac{\partial}{\partial x_1}(h_3 B_3) + \frac{B_2}{\rho h_2}\frac{\partial}{\partial x_2}(h_3 B_3)\right] , \quad (40)$$

$$\frac{\partial}{\partial t}(h_3 B_3) = (h_3)^2\left[B_1 \frac{\partial}{\partial x_1}\left(\frac{v_3}{h_3}\right) + \frac{B_2}{h_2}\frac{\partial}{\partial x_2}\left(\frac{v_3}{h_3}\right)\right] . \quad (41)$$

Then, subtracting (adding) these equations leads to the characteristic equation along the forward (backward) characteristic C^+ (C^-),

$$\frac{D}{Dt}\left(\frac{v_3}{h_3}\right) \mp \left(\frac{1}{h_3}\right)^2 \frac{1}{\rho^{1/2}}\frac{D}{Dt}(h_3 B_3) = 0 . \quad (42)$$

In equation (42), the comoving derivatives along C^+ and C^- are defined by equation (32) (or eq. [33]) for waves propagating in the 2-direction (or 1-direction), since as described previously the source step is applied in a Lagrangean frame of reference. These equations are similar to those used for Alfvén waves in the poloidal directions (eqs. [20] and [22]). Physically, they state that along characteristics of the wave motion, changes in the fundamental quantities of angular velocity and magnetic flux are related via equation (42).

We can difference the characteristic equations in a similar manner as was described in § 3.2.2, except now we use the rotational velocity, $\Omega \equiv v_3/h_3$, and the magnetic flux, $\Phi \equiv h_3 B_3$, as the dependent variables. Differencing along the for-

ward and backward characteristics in one dimension leads to the two coupled equations

$$(\Omega_i^{*,n+1/2} - \Omega_i^{+,n}) - (\Phi_i^{*,n+1/2} - \Phi_i^{+,n})/(h_3^2 \rho^{1/2})_i^+ = 0 , \quad (43)$$

$$(\Omega_i^{*,n+1/2} - \Omega_i^{-,n}) + (\Phi_i^{*,n+1/2} - \Phi_i^{-,n})/(h_3^2 \rho^{1/2})_i^- = 0 , \quad (44)$$

where the $\Omega_i^{-,n}$ and $\Phi_i^{-,n}$ are the upwind interpolated values at the old time level at the footpoints of the C^- characteristic, $\Omega_i^{+,n}$ and $\Phi_i^{+,n}$ are the upwind interpolated values at the old time level at the footpoints of the C^+ characteristic, while the $\Omega_i^{*,n+1/2}$ and $\Phi_i^{*,n+1/2}$ are the advanced time values located at zone interfaces (as in Fig. 3). The denominator of the second term in each of these equations is time centered by choosing values for h_3 and ρ which are appropriate to the midpoint of each characteristic. The two coupled linear equations (43)–(44) can then be solved directly yielding $\Omega_i^{*,n+1/2}$ and $\Phi_i^{*,n+1/2}$. These time advanced interface values are then used in a finite difference update of the actual evolution equations (36)–(37).

For our two-dimensional simulations, we use a directionally split algorithm, i.e., we first update v_3 and B_3 due to torsional Alfvén wave motion in the 1-direction, followed by an identical update in the 2-direction. We proceed by solving at every grid point equations (43) and (44) for $\Omega_{i,j}^{*,n+1/2}$ and $\Phi_{i,j}^{*,n+1/2}$ by computing the upwind variables at the footpoints from the characteristic speeds $\pm B_1/\rho^{1/2}$. These partially updated values are used in the 1-direction evolution equations

$$\frac{v3_{i,j}^{n+a} - v3_{i,j}^n}{\Delta t} = \frac{(B1_{i,j} + B1_{i+1,j})}{2g31b_{i,j}d_{i,j}dx1a_i}(\Phi_{i+1,j}^{*,n+1/2} - \Phi_{i,j}^{*,n+1/2}) , \quad (45)$$

$$\frac{B3_{i,j}^{n+a} - B3_{i,j}^n}{\Delta t}$$
$$= \frac{(B1_{i,j} + B1_{i+1,j})g31b_i}{2dx1a_i}(\Omega_{i+1,j}^{*,n+1/2} - \Omega_{i,j}^{*,n+1/2}) . \quad (46)$$

We then repeat this process for Alfvén waves in the 2-direction, by solving at every gridpoint equations (43) and (44) for $\Omega_{i,j}^{*,n+1/2}$ and $\Phi_{i,j}^{*,n+1/2}$ by computing the upwind variables at the footpoints from the characteristic speeds $\pm B_2/\rho^{1/2}$. These partially updated values are used in the 2-direction evolution equations

$$\frac{v3_{i,j}^{n+1} - v3_{i,j}^{n+a}}{\Delta t}$$
$$= \frac{(B2_{i,j} + B2_{i,j+1})}{2g32b_jd_{i,j}g2b_idx2a_j}(\Phi_{i,j+1}^{*,n+1/2} - \Phi_{i,j}^{*,n+1/2}) , \quad (47)$$

$$\frac{B3_{i,j}^{n+1} - B3_{i,j}^{n+a}}{\Delta t}$$
$$= \frac{(B2_{i,j} + B2_{i,j+1})g32b_j}{2g2b_idx2a_j}(\Omega_{i,j+1}^{*,n+1/2} - \Omega_{i,j}^{*,n+1/2}) . \quad (48)$$

Again, we expect this directional splitting to lead to diffusion of the Alfvén wave across field lines in the downwind direction, but for staggered meshes this diffusion is probably unavoidable to some degree. Whether a more sophisticated algo-

rithm can reduce the diffusion is a subject for future numerical testing, however such development should not change the basic premise on which the MOC update is based. Note that the MOC algorithm described in this section is appropriate only for $2\frac{1}{2}$-dimensional simulations. In three dimensions, the full MOC-CT scheme must be used to evolve all three components of the field.

Once the MOC update of the source terms is completed, we can advect of these quantities. The rotational velocity is advected like a zone centered scalar, and this update, including the finite difference equations, has already been described in Paper I. For the toroidal component of the magnetic field, B_3, we advect the magnetic flux rather than the field itself. Thus, we update equation (39) using a directionally split algorithm, by first advecting the magnetic flux in the 1-direction using

$$\mathscr{F}_{i,j}^1 = \dot{M}_{i,j}^1(B3/d)_{1,i,j}^* g2a_i^{n+1/2} , \quad (49)$$

$$(B3_{i,j}^{n+1}g2b_i^{n+1}dx1a_i^{n+1} - B3_{i,j}^n g2b_i^n dx1a_i^n)/\Delta t$$
$$= -(\mathscr{F}_{i+1,j}^1 - \mathscr{F}_{i,j}^1) , \quad (50)$$

where $(B3/d)_{1,i,j}^*$ represents the face centered and upwinded value resulting from one of the three interpolation algorithms in ZEUS-2D (donor cell, van Leer, or PPA). We then advect the magnetic flux in the 2-direction using

$$\mathscr{F}_{i,j}^2 = \dot{M}_{i,j}^2(B3/d)_{2,i,j}^* , \quad (51)$$

$$(B3_{i,j}^{n+1}g2b_i^n dx2a_j^{n+1} - B3_{i,j}^n g2b_i^n dx2a_j^n)/\Delta t$$
$$= -(\mathscr{F}_{i,j+1}^2 - \mathscr{F}_{i,j}^2) . \quad (52)$$

Note that by using the mass flux variables $\dot{M}_{i,j}^1$ and $\dot{M}_{i,j}^2$ defined by eqs. (55)–(56) in Paper I, and interpolating on B_3/ρ rather than B_3 itself, we have used consistent transport to try to minimize the diffusion of the toroidal magnetic field relative to the mass, as required by flux-freezing.

3.4. *Boundary Conditions*

As stated in § 3.2.1, the CT scheme guarantees a divergence-free field only if the initial field is divergence-free, and that no monopoles are introduced through the boundary conditions. In general, divergence-free boundary conditions are nontrivial to construct. Thus, in ZEUS-2D we have chosen not to apply boundary conditions to the field components themselves, but to the EMFs instead. We then update the field components in the ghost zones using the actual difference equations. Since the EMF is corner centered, the two rows of ghost zones in which we specify the EMF lie beyond the boundary, i.e., at $i = iim1$ and $i = iim2$ for the inner i boundary, $i = iop2$ and $i = iop3$ for the outer i boundary (see Fig. 1 of Paper I), and similarly for the inner and outer j boundaries. Values for the EMF at $i = ii$ and $i = iop1$ (or $j = ji$ and $j = jop1$) are computed from the difference equations. For the CT algorithms, we have implemented all of the same types of boundary conditions for the EMFs that are used for the HD variables described in Paper I. Although in ZEUS-2D the only nonvanishing component of the EMF vector is the 3-component (which is always tangential to the boundaries), we cannot use the boundary conditions applied for the HD for tangential vectors directly to the EMF.

Instead, since the EMF is formed by the product of two more fundamental variables (the velocity and the magnetic field), we must examine the consequences of the boundary condition on these variables and their effect on the EMF vector. Thus, the appropriate boundary conditions to be used are the following:

1. *Reflecting Boundary Condition.*—The normal components of velocity and magnetic field are reflected, while the tangential components are continuous. This implies the EMF in the ghost zones are equal to the negative of the EMF in the equivalent active zones.

2. *Inflow Boundary Condition.*—The EMF in the ghost zones are set to some predetermined value, which may be allowed to vary in time.

3. *Outflow Boundary Condition.*—The EMF in each ghost zone are set equal to the EMF in the first active zone.

4. *Periodic Boundary Condition.*—The EMF in the ghost zones are set equal to the EMF in the corresponding active zones on the opposite side of the grid.

In addition to these boundary conditions, we have also implemented a condition in which velocity is reflected, while the normal component of the magnetic field is continuous and the tangential component is reflected. This condition is designed for symmetry planes (such as equatorial symmetry).

For the unconstrained toroidal magnetic field components, we can apply boundary conditions directly. Thus, we use the same HD boundary conditions with one important exception. For outflow boundaries, perfectly transparent boundary conditions for outgoing Alfvén waves can be achieved by removing the incoming characteristic from the evolution equation at the boundary (Thompson 1987; Vanajakshi, Thompson, & Black 1989). Numerically, this can be achieved by setting the gradients of all quantities along the incoming characteristic to zero. Thus, for outflow boundaries, we project the angular velocity and toroidal magnetic field to achieve perfect transparent boundaries for outgoing torsional Alfvén waves. In addition, at an equatorial plane of symmetry the toroidal field should be antireflected while the rotational velocity is merely reflected.

As with the HD boundary conditions, the MHD boundary conditions can be applied independently for each ghost zone on the mesh. The boundary conditions for each variable are also implemented in a different subroutine, which can be called from anywhere in the code, to allow for more modular programming and the rapid modification of the numerical boundary conditions.

3.5. *Incorporating MHD into ZEUS-2D*

Most of the MHD algorithms described in this chapter can be built into self-contained modules. Modifying ZEUS-2D to perform MHD calculations is then simply a matter of calling these modules at the appropriate points in the program control sequence. Figure 4 shows how the schematic flow chart of ZEUS-2D, originally presented in Figure 7 of Paper I, is modified by the inclusion of the MHD algorithms. To account for changes in the equation of motion due to Lorentz forces, we must modify "Substep 1" of the source step to include the finite-difference terms (eqs. [26]–[29]). The MOC update of the coupled toroidal component of the magnetic field and ve-
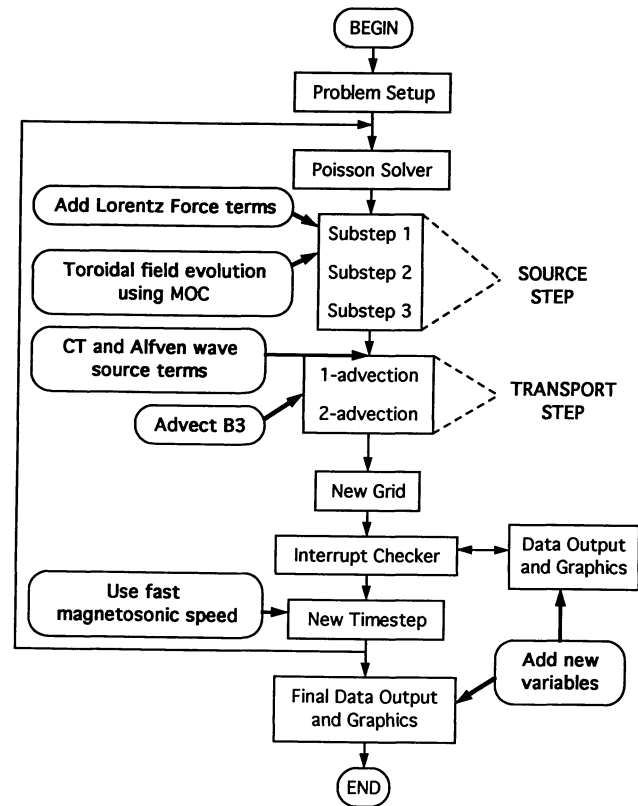

FIG. 4.—Schematic flow chart of the ZEUS-2D code which diagrams the changes required to add the magnetohydrodynamical algorithms to the hydrodynamical algorithms. Compare this figure to Fig. 7, Paper I.

locity is performed in a module called at the end of "Substep 1" of the source step, but before "Substep 2." The MOC-CT evolution of the poloidal field components (eqs. [11]–[12]) is performed at the start of the transport step. The partially updated MOC magnetic field values $B_1^{r,n+1/2}$ and $B_2^{r,n+1/2}$ located at cell corners are used to update velocities according to equations (30) and (31). The transport module must also be modified to incorporate the advection terms for B_3 using equations (49)–(52). An additional important modification is the inclusion of MHD wave speeds in the explicit CFL stability criterion (Paper I). For MHD simulations, the CFL condition must be modified so that

$$\Delta t \le \min (\Delta x)/(|u| + C_f), \qquad (53)$$

where u is the local fluid velocity and C_f is the fast magnetosonic speed ($C_f^2 = v_A^2 + C_a^2$), where v_A and C_a are the Alfvén and sound speeds, respectively). Thus, since $C_f > C_a$, the HD CFL condition may not be a sufficient stability criterion for strong fields. We replace the limiting time step δt_1, defined by equation (75) in Paper I, by the above for MHD simulations. Finally, we must of course modify the data output and graphics routines to plot the new variables.

As described in Paper I, we use the precompiler CPP for source code management and to control the compilation steps of ZEUS-2D. All of the above changes, including the inclusion of the appropriate modules, are controlled by conditional

compilation macros, which include or suppress references to the MHD variables and subroutines. This allows an optimized version of the code to be generated for both HD and MHD simulations.

4. THE MAGNETOHYDRODYNAMIC TESTS

The MHD algorithms in the ZEUS-2D code are not simply a new implementation of old methods, but instead incorporate some entirely new numerical methods. Performing an extensive series of tests for these algorithms is therefore even more important than for the HD algorithms. However, unlike HD codes, the development and application of MHD codes for problems in astrophysics is a relatively new area of research. In this work, therefore, we have assembled a new collection of test problems that includes problems of various complexity, from one-dimensional advection problems to full two-dimensional simulations. Indeed, for some of these latter tests, the distinction between test problem and application becomes vague. We describe the results obtained with the ZEUS-2D code for these test problems below. In addition, the setup and execution of each of the test problems is described in greater detail in Stone et al. (1992) so that other researchers can use this test suite to calibrate other codes.

4.1. *Cartesian Advection Tests*

The simplest test we have performed is the one-dimensional advection of a square pulse of transverse magnetic field (a double current sheet), a test which was originally described by EH. Like the HD advection tests (see § 5.1 of Paper I), the problem is constructed by ignoring the source terms in the dynamical equations and assuming a stationary velocity field. However, since the CT scheme does not operator split the induction equation, but uses the EMF to update the magnetic fluxes due to both the transport and source terms all at once, we must also ensure that the parallel component of the magnetic field is zero to prevent the generation of Alfvén waves. Initially, the pulse is 50 zones wide and centered at $x = 30$, and the test is stopped when the pulse has been advected a distance of 5 times its width. Figure 5 gives the results of advecting a pulse of B_2 in the 1-direction using three advection algorithms: van Leer, PPA, and PPA with the steepener (identical results are obtained by advecting a pulse of B_1 in the 2-direction). If we compare these results to those for the HD advection tests (Fig. 8 in Paper I), we find exact agreement point for point between the two. Of the three schemes tested here, we find the van Leer scheme is the most diffusive (with discontinuities kept to about 14 zones wide), while PPA with the steepener is the best (discontinuities are kept to only two zones wide). These results are also comparable to those given by EH.

We also plot in Figure 5 the 3-component of the electric current density for each advection method. Analytically, the current density should be a delta function located at the pulse edges. However, the diffusivity inherent in each scheme gives the peaks finite width. As we increase the order of the advection scheme, from van Leer to PPA with the steepener, the peaks become narrower and higher as expected. The main significance of the numerical results for the current densities, however, are that they show no anomalous sign reversals. As demonstrated by EH, MHD algorithms based on evolving the

vector potential can produce nonmonotonic currents, which will couple directly to the dynamics through the Lorentz force term and can produce results of unknown reliability. The real advantage of the CT scheme over vector potential methods is that one need not take a second derivative to obtain the currents.

We have also performed a one-dimensional Cartesian test for a square pulse of the 3-component of the magnetic field in both directions. Once again, the results are identical point for point with the HD and CT Cartesian advection tests.

4.2. *MHD Riemann Problem*

We can increase the complexity of our tests with a one-dimensional dynamical problem which tests both the transport and source terms. We have found the MHD analog of the Sod shock tube problem, described by Brio & Wu (1988, hereafter BW) is an excellent test. Unlike the HD case, however, the MHD Riemann problem possesses no known analytic solution. Part of the difficulty in solving the MHD equations analytically arises because they are nonconvex (unlike the Euler equations which are convex), a point first proven by BW. These authors give an excellent discussion of the mathematical significance of the nonconvexity of the MHD equations. Physically, however, this nonconvexity means that different waves of the same family can have the same propagation velocity. Thus, in MHD flows, one can have compound waves, consisting of a rarefaction wave attached to a shock of the same family (e.g., a slow rarefaction wave attached to a slow shock wave, etc.). This behavior is markedly differently from HD flows, and furthermore it disproves the usual belief that magnetosonic waves are just like sound waves in the Euler equations.

Like the HD Sod shock tube problem, the MHD Riemann problem features two initially discontinuous states that interact. BW choose a $\gamma = 2.0$ gas and left and right states consisting of $p_l = 1.0$, $\rho_l = 1.0$, $(B_x)_l = 0.75$ and $(B_y)_l = 1.0$ and $p_r = 0.1$, $\rho_r = 0.125$, $(B_x)_r = 0.75$, $(B_y)_r = -1.0$. The problem is initialized on a domain of $x \in (0, 800)$, using 800 zones. At $t = 0$ the discontinuity is located at $x = 400$. The problem is run to $t = 80$. The discontinuity is initially located at a cell interface. Note that the choices for the dynamical variables are identical to those in the Sod shock tube problem, except a magnetic field which possesses a kink at the discontinuity is added. The angle that the magnetic field lines make with the shock normal is given by $\tan \theta = (0.75)^{-1}$.

BW present numerical solutions to this problem using four methods, Lax-Friedrichs, Lax-Wendroff, flux-corrected transport, and a second-order upwind scheme designed for this problem. Since there is no analytic solution, we will compare our numerical results with those of BW for their second order upwind scheme (given in their Fig. 2). Figure 6 shows the ZEUS-2D results for every dependent variable in the problem (density, pressure, B_y, and v_x and v_y). Examination of the these results reveals the complexity of the MHD Riemann problem as compared to its HD counterpart. One can identify the following components in the solution. The waves moving to the left are a fast rarefaction fan and a slow compound wave (consisting of a slow rarefaction attached to a slow shock), while the waves moving to the right are a contact discontinuity, a slow shock and a fast rarefaction fan. The appearance of
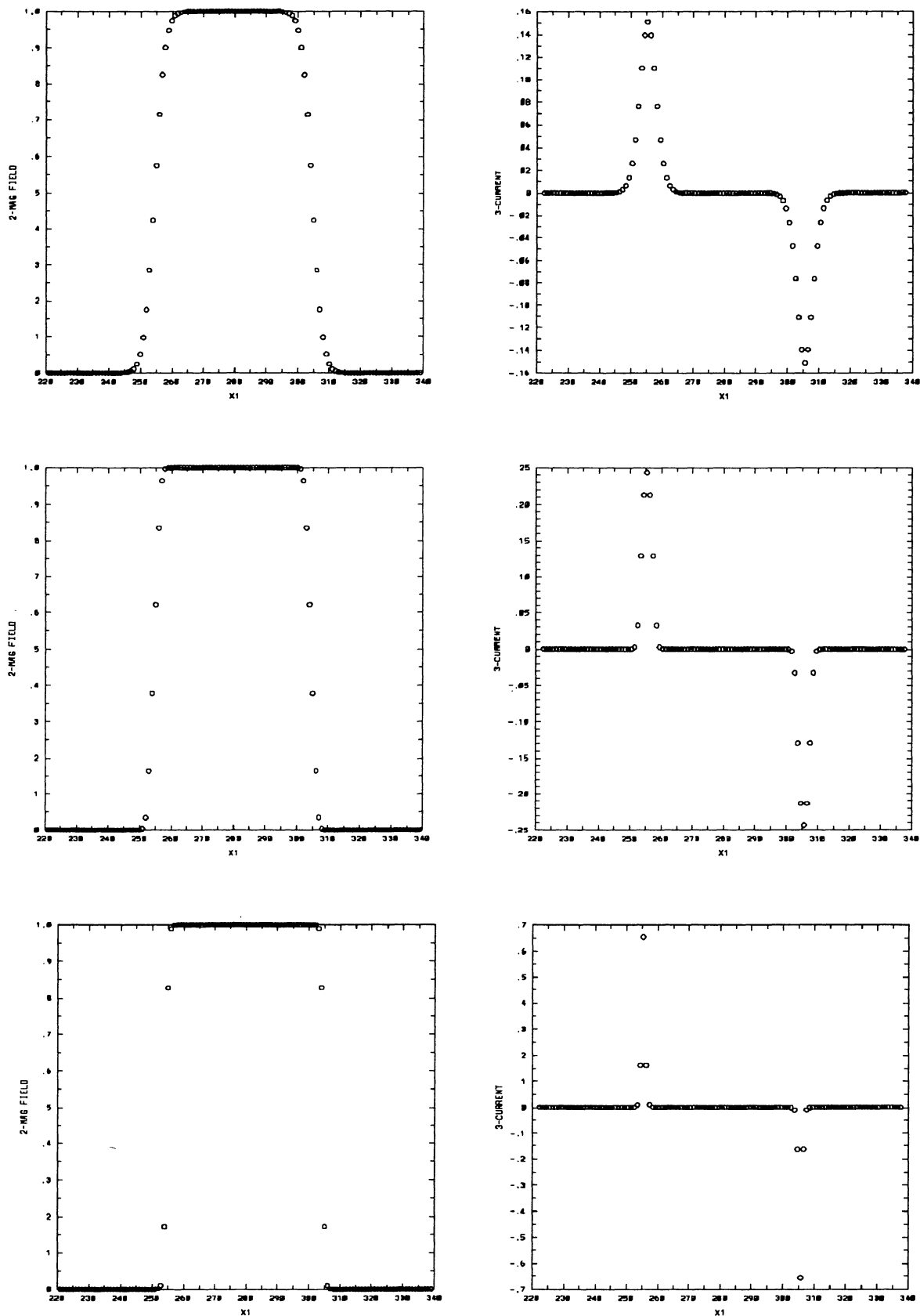
FIG. 5.—Results for the Cartesian advection of a square pulse of transverse field, originally 50 zones wide, after traversing a distance of 250 zones using the van Leer (*top*), PPA (*middle*), and PPA with steepener (*bottom*) interpolation algorithms. On the left are plotted the resulting pulse shapes, on the right are the 3-component of the electric current density in each case. Note the latter show no anomalous sign reversals. Analytically, the pulse edges should be located at $x = 255$ and $x = 305$.

802
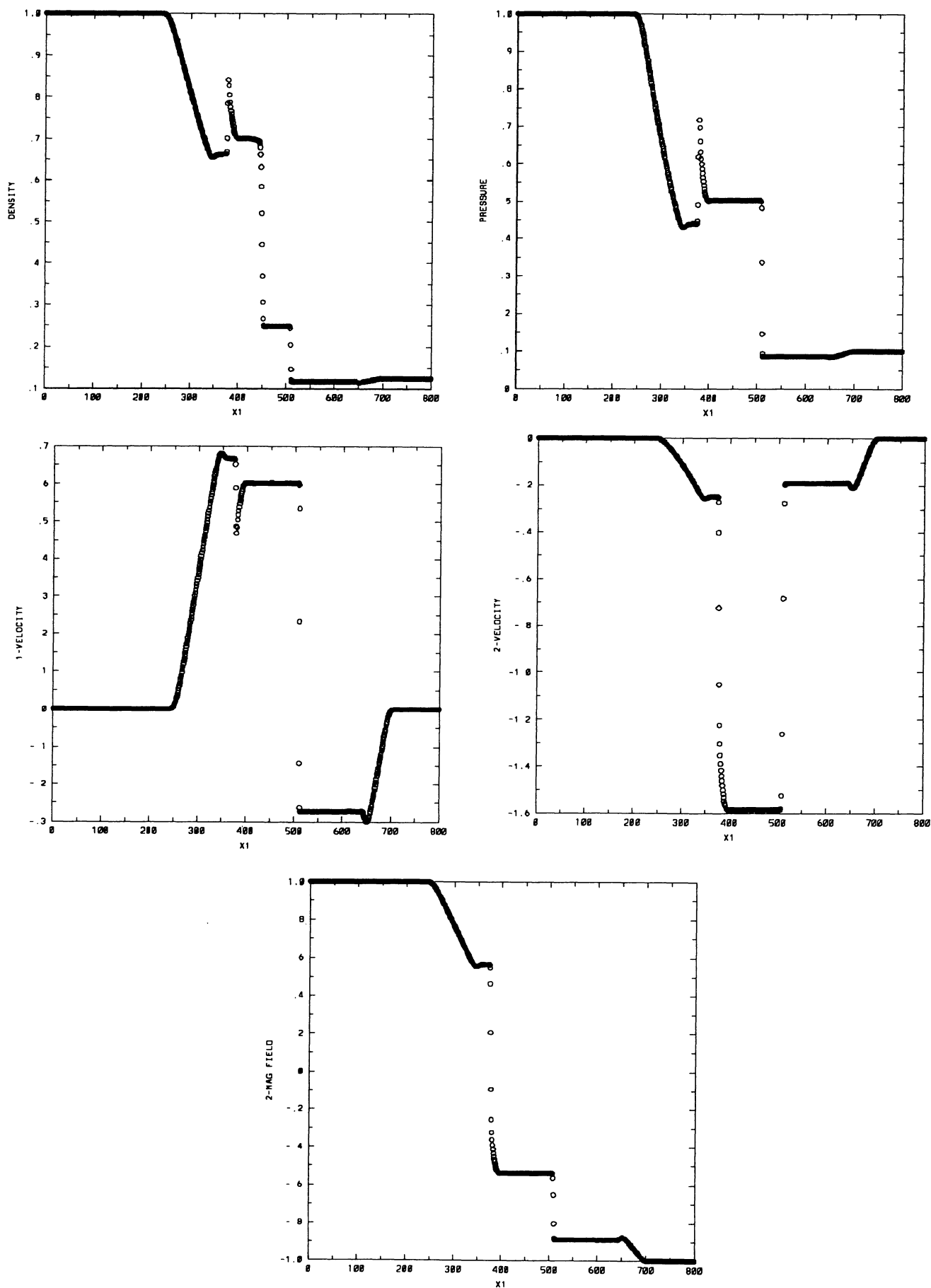
FIG. 6.—Results for the MHD Riemann problem as computed using ZEUS-2D with 800 zones and the van Leer advection algorithm. These results are to be compared with those of Brio & Wu (1988, Fig. 2).

the compound wave in the solution demonstrates the nonconvex nature of the MHD equations, as described above. A comparison of the numerical solution generated by ZEUS-2D with the BW numerical result shows excellent qualitative agreement with respect to the positions and widths of the various features in the solution. The only serious discrepancy occurs at the foot of the fast rarefaction fan propagating in each direction where the ZEUS-2D solution shows an anomalous under or over shoot. We can attribute this to the fact that although we have built a numerical scheme which is upwind in the Alfvén wave characteristics, it is not upwind in the magnetosonic characteristics. This situation is identical to the HD, where overshoots can occur at rarefaction fans for sound waves. Constructing a scheme which is upwind in all the characteristics (such as the BW method) removes this overshoot, but results in a much more complex and slower algorithm. The ZEUS-2D result is substantially better that the results for the Lax-Wendroff, Lax-Friedrichs, and flux corrected transport schemes presented in BW (their Figs. 3, 4, and 6, respectively). Thus, using the relatively simple methods in ZEUS-2D, we find that we can achieve results that are near those for a much more complex, fully upwind algorithm.

4.3. The Weber-Davis Wind Solution

Another one-dimensional dynamical test problem, originally suggested to us by J. Hawley, is the semi-analytic solution for a magnetic stellar wind due to Weber & Davis (1967, hereafter WD). This problem was first studied in the context of magnetic braking of stellar rotation to account for the transition along the main sequence from rapid to slow rotators around the spectral type F5. The original WD models are one-dimensional (valid only at the equatorial plane), but recently Sakurai (1985) has outlined a method of obtaining the two-dimensional structure of these winds. However, since the two-dimensional solutions are very difficult to obtain, we shall concentrate on testing with the original one-dimensional WD models.

The method of obtaining the WD solution for a magnetic wind has been reviewed in detail by Sakurai (1985). By assuming a steady, one-dimensional flow, the MHD equations are reduced to a set of four algebraic equations expressing conservation of mass, angular momentum, total energy and magnetic flux, combined with a polytropic equation of state and a flux freezing condition that relates the radial and toroidal components of the magnetic field and velocity. This set of equations can be reduced algebraically to the Bernoulli equation which determines the density profile, namely

$$H(r, \rho) = E . \qquad (54)$$

Given a value for the parameter E (the total energy in the wind), the density profile is then a level contour of the Bernoulli function $H(r, \rho)$. The topology of the Bernoulli function is similar to that resulting for HD winds, except now the solution plane contains three critical points where solution curves can cross: the slow, Alfvén, and fast points. Physically these critical points represent the positions in the flow where the radial velocity equals the slow, Alfvén and fast wave speeds, respectively. The Bernoulli function $H(r, \rho)$, and there-

fore the WD wind solutions, are uniquely determined by three parameters, γ, the exponent of the polytropic equation of state, Θ, the ratio of thermal to gravitational potential energy at the Alfvén point, and ω, the ratio of rotational to gravitational potential energy at the Alfvén point. Given a set of these parameters, the only physically acceptable solution is the single level curve which passes through all three critical points smoothly with a monotonically decreasing density profile; all others violate entropy considerations or zero pressure boundary conditions at infinity. Since the Bernoulli function is nonlinear and quite complicated, analytic solutions for this level curve are not possible. Instead, numerical root finding methods must be used to trace the proper solution through every radial point. Great care must be taken to ensure the numerical scheme finds the single physically correct root at all radial points, and does not diverge onto unadmissible roots. This task is nontrivial, especially at the critical points where the roots cross. We do not give the details of our numerical technique for computing the WD solution for a magnetic wind here, it is given in Stone et al. (1992).

Once we have a WD wind solution, it can be used to test the ZEUS-2D code in two ways. We can either (1) initialize the WD solution over the entire computational domain and check that ZEUS-2D can hold this solution stably, or (2) we can introduce the WD solution as boundary conditions at the inner radial boundary, with vacuum conditions everywhere else on the grid, and check that ZEUS-2D can generate the correct solution over the whole grid from these boundary values. We have performed both kinds of tests with ZEUS-2D and found identical results, provided that one waits long enough in the latter case for all transients to die away (typically about 10 fluid crossing times are needed). We present the results for two different WD solutions below. These solutions are all generated using a strip of 100 radial zones in spherical polar geometry centered on $\theta = \pi/2$. The evolution is stopped in each case after several fluid crossing times, which should give any potential difficulties ample time to grow. We have checked that the solutions at later times do not differ significantly from those presented here.

The first test solution is for the values of the parameters given by Sakurai (1985), namely $\gamma = 1.2$, $\Theta = 0.5$ and $\omega = 0.25$. This solution is particularly attractive since with these values for the parameters, all three critical points are well separated in solution space. Figure 7 shows the solution for these parameters in the domain $r \in (0.5, 3.0)$. The numerical solution (open circles) is plotted over the semi-analytic solution (solid line) given by the root finding techniques described above. The positions of the slow, Alfvén, and fast points are denoted by S, A, and F on these curves.

The solution is characterized by monotonically decreasing density, internal energy and radial and azimuthal magnetic field. The rotational velocity peaks near the inner boundary then decreases, while the radial velocity is steadily increasing. Physically, the solution represents radial acceleration of the wind via magnetic stresses. Note that while both the radial and azimuthal magnetic field components are monotonically decreasing, they scale as $B_r \propto r^{-2}$ and $B_\phi \propto r^{-1}$, respectively, so that the field is purely radial at the base of the wind (stellar surface), and becomes increasingly azimuthal as it is swept back by the rotating flow at larger radii. For all variables except
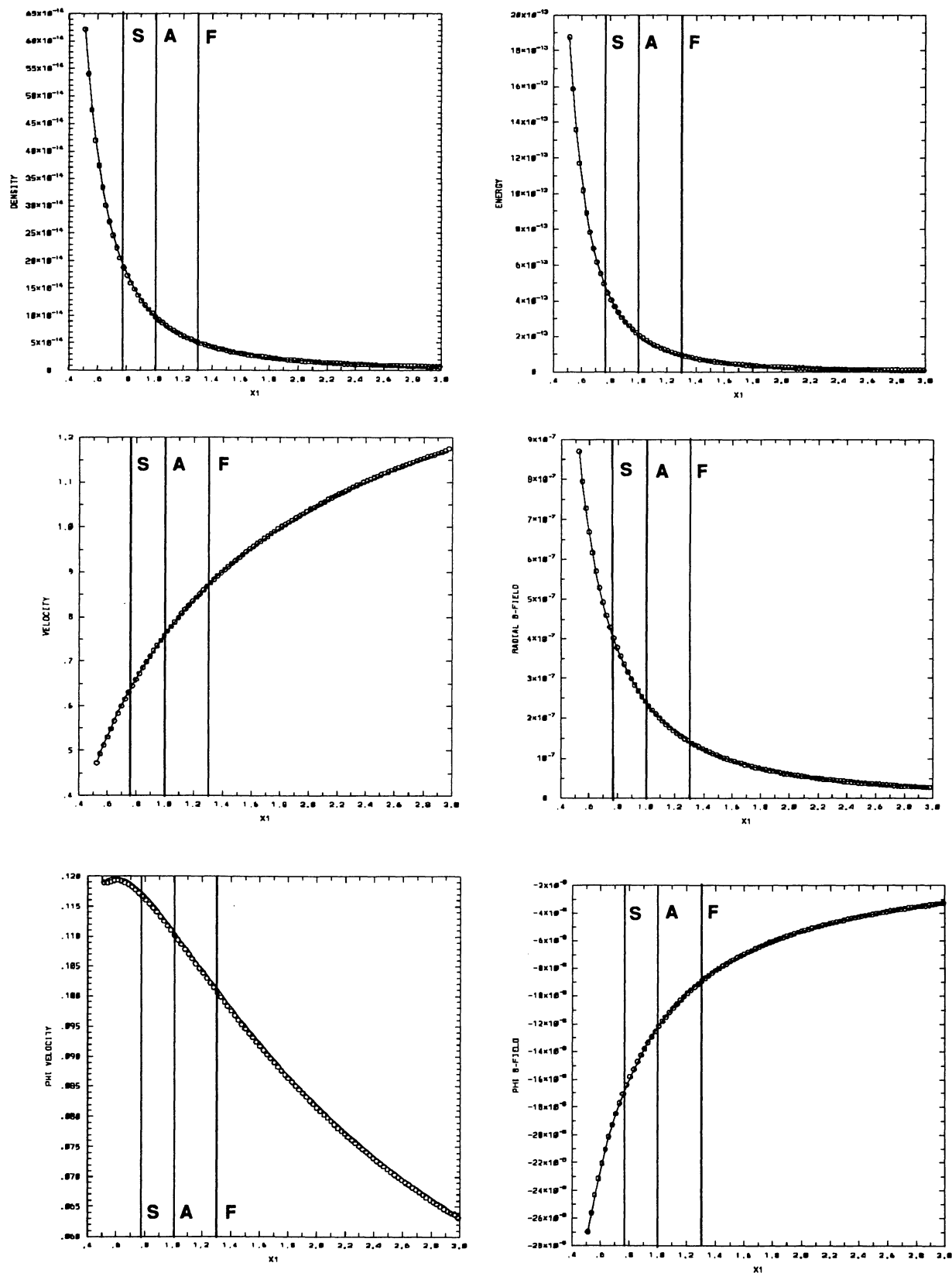
FIG. 7.—Weber-Davis solution to a magnetic stellar wind using values for the parameters of $\gamma = 1.2$, $\Theta = 0.5$, and $\omega = 0.25$. The solution computed by ZEUS-2D (*open circles*) is plotted over the solution computed by semi-analytic root finding methods (*solid line*) in each case. The locations of the slow, Alfvén, and fast critical points are denoted by the vertical lines labeled S, A, and F, respectively.
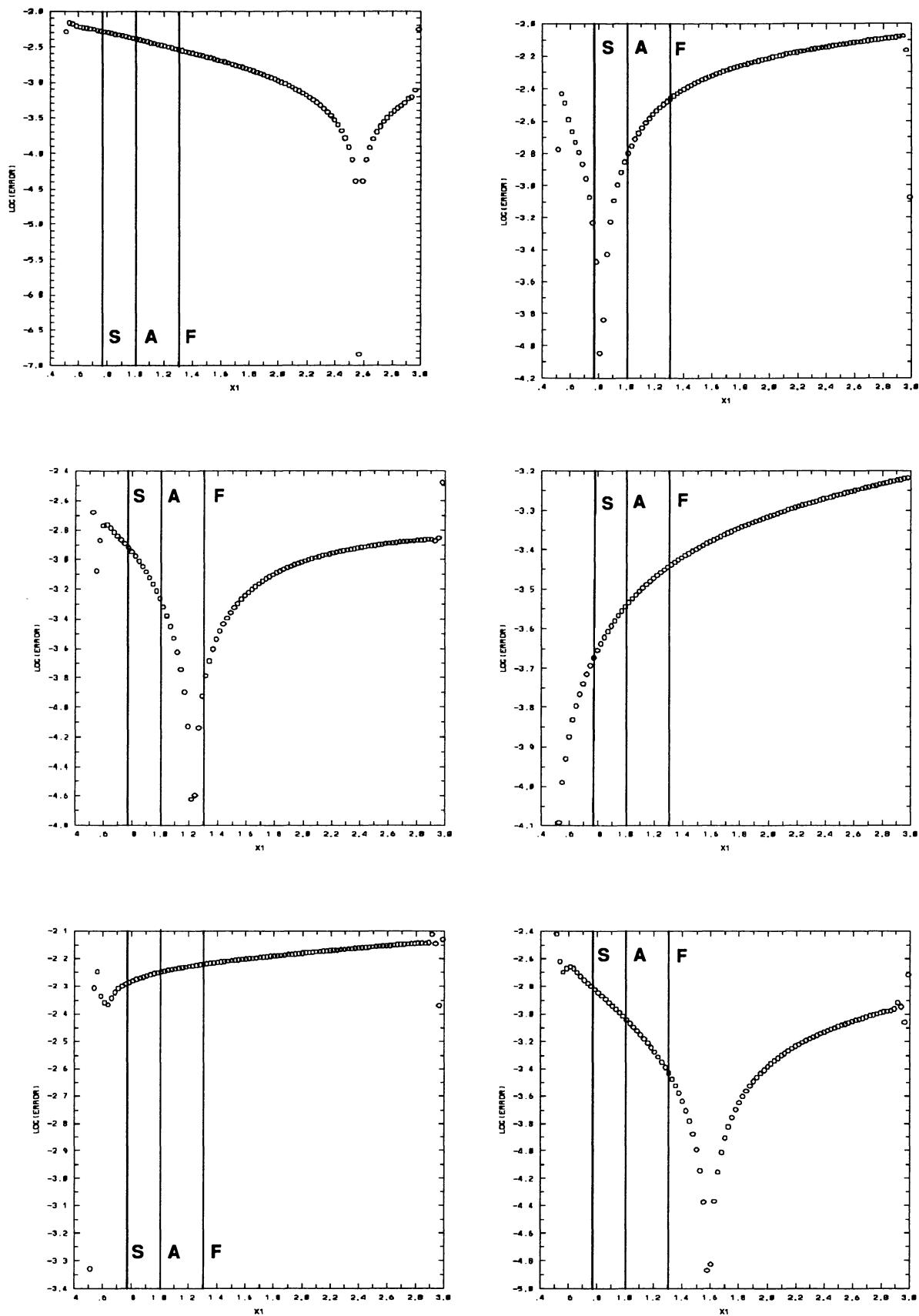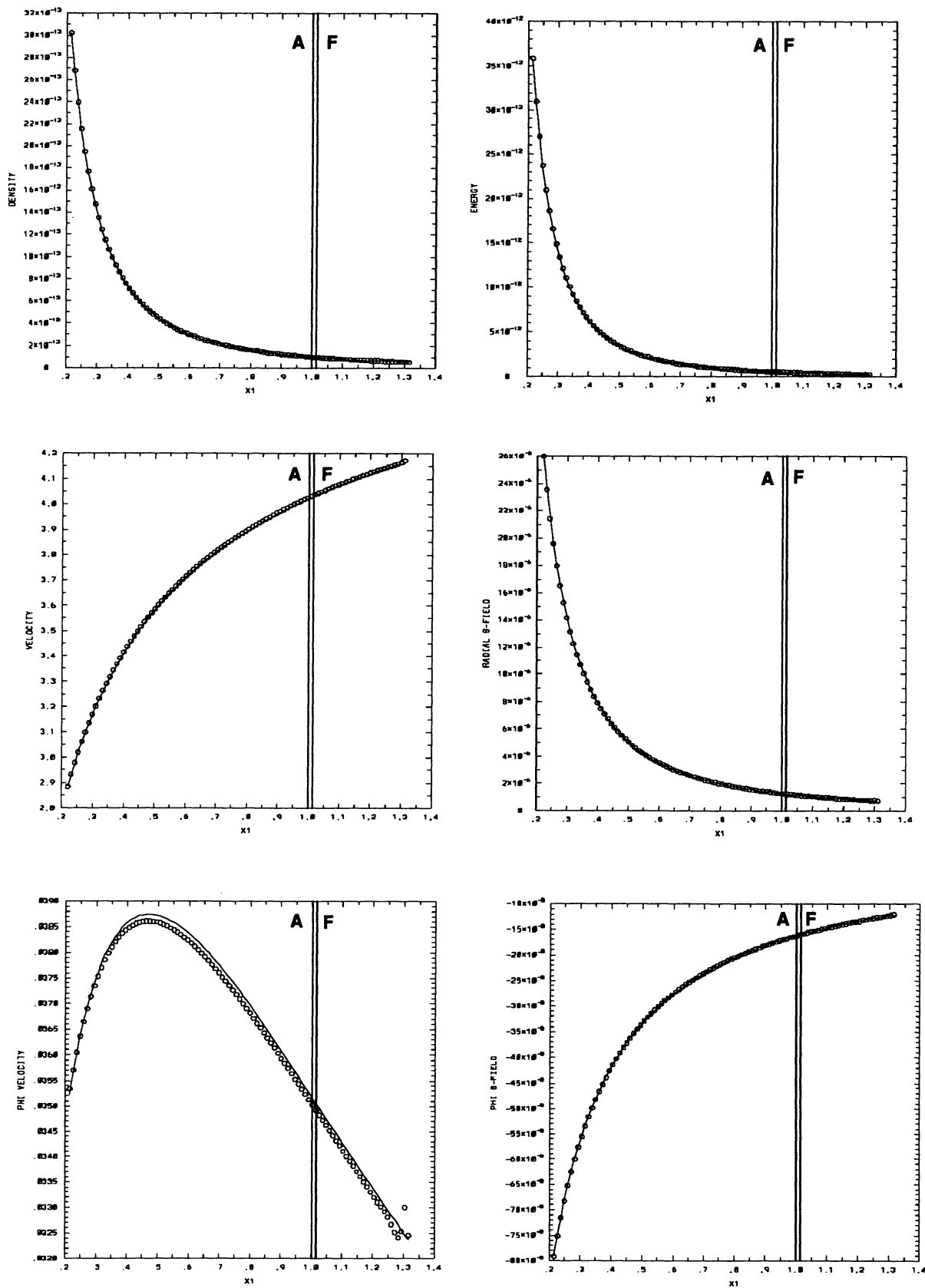
Fig. 8.—Relative errors in the Weber-Davis wind solution shown in Fig. 7

806

FIG. 9.—Weber-Davis solution to a magnetic stellar wind using values for the parameters of $\gamma = 1.22$, $\Theta = 1.5$, and $\omega = 0.3$. The solution computed by ZEUS-2D (*open circles*) is plotted over the solution computed by semi-analytic root finding methods (*solid line*) in each case. The locations of the slow, Alfvén, and fast critical points are denoted by the vertical lines labeled S, A, and F, respectively.

807

the rotational velocity, the numerical solution follows the analytic solution very closely. The logarithm of the relative errors for each variable, given in Figure 8, show that even for the v_ϕ, the relative errors are all less than 1% over the whole grid. Dips in the errors are positions where the sign of the error changes. For all variables, including the rotational velocity, the greatest error occurs at the first few points near each boundary. We assert that this results from the fact that the numerical solution in the ghost zones is held fixed at the analytic values, while finite-differencing errors causes the numerical solution in the active zones to relax slightly away from the analytic solution (to one that satisfies the finite-difference equations to truncation error). Thus, near the boundaries, the slope of numerical solution gains significant error. This behavior can be traced in the solution for the rotational velocity, where the numerical solution undergoes a sharp dip at the inner boundary (where the slope of the solution is incorrect), and thereafter traces the analytic solution very closely, although with the wrong amplitude.

We have also tested the ZEUS-2D code with a WD solution using the original set of parameters chosen by WD, namely $\gamma = 1.22$, $\Theta = 1.5$, and $\omega = 0.3$. These values are appropriate for the solar wind. They give very closely spaced Alfvén and fast points, whereas the slow point is located deep in the solution, at very small radii. Since at such small radii the slope of the solution curve is very large at the slow critical point, obtaining the analytic solution through this point via the root finding techniques we are using becomes very difficult. As such, we choose to test ZEUS-2D on the domain $r \in (0.2, 1.3)$, which excludes the slow point which is located at $r = 0.11$. The ZEUS-2D solution for this choice of parameters, plotted over the analytic solution, is given in Figure 9, while Figure 10 gives the errors in the solution. We again find excellent agreement between the analytic and numerical solutions, except for the rotational velocity. Even for this variable, the maximum error is only about 1%. We again attribute this error to incorrect slopes at the inner boundary, which in this case are more serious since the slopes are steeper at such small radii.

We emphasize that we have found identical results, even for the errors, regardless of whether we initialize the solution on the grid, or allow the solution to be generated via boundary conditions. Furthermore, we find that the time-dependent ZEUS-2D codes trace the correct solution through the critical points, even if the lower boundary is located in the submagnetosonic portion of the wind. The code gives the correct acceleration of the flow from submagnetosonic inflow to supermagnetosonic outflow. The WD wind solution is an excellent test of the rotational terms in the dynamical equations, since the wind is dominated by the interaction of the inertia of the rotating wind sweeping back the radial field lines. The test is also very relevant to our intended application of ZEUS-2D to magnetically driven winds from disks and protostars. Moreover, by performing time-dependent simulations (as a test problem), we have also demonstrated the stability of the one-dimensional wind solution!

Since the WD wind solution contains no discontinuities, it is an excellent problem with which to perform convergence testing. By convergence, we mean the rate at which the error in the numerical solution as compared to the correct solution (given

either by an analytic solution, or an infinitely high-resolution numerical result), decreases as a function of the number of grid points. (This type of convergence has no relation to the convergence rate of an iterative scheme for solving sets of linear or nonlinear equations.) Hawley (1989) has defined three basic types of convergence testing.

1. *Single–time step convergence testing.*—The analytic solution is initialized on the grid and evolved for one time step, then the absolute error per unit time over the entire grid is computed from

$$\epsilon = \frac{1}{N} \sum_{i=1}^{N} |X_i(\Delta t) - \tilde{X}(\Delta t)| \Big/ \Delta t \qquad (55)$$

where X_i is the numerical solution, $\tilde{X}$ the analytic solution, N the number of grid points, and Δt the time step. This is repeated for various resolutions. The change in the error with different resolutions then gives the convergence rate (slope of the log − log graph).

2. *Extended evolution convergence testing.*—An analytic solution is initialized on the grid and evolved to a fixed time. The error is computed as above (except we do not divide by Δt), and the results from different resolutions give the convergence rate.

3. *Self-convergence testing.*—The results from (2) may be very poor since something (e.g., boundary conditions) may prevent the code from converging to the analytic solution. However, the code may still be converging, albeit to a numerical solution for the specified problem which is different from the intended analytic solution. We can still measure the correct convergence rate of the code by doing self-convergence testing. The procedure is to run the code to some fixed time, for two different resolutions, and compute the relative change in all the variables between the two resolutions. A convergence rate is computed by using a third resolution, and comparing the change in the two errors over the three different resolutions.

The advantage of the first technique is that it is very cheap to carry out, and can therefore be used for very high resolutions. Moreover, in one time step, the effects of individual terms in the equations can be singled out (e.g., the error in density must be due exclusively to advection). By ignoring points near the boundaries, errors generated by the boundary conditions can also be eliminated for an explicit code. We have already used the second technique to test the convergence rate of the advection algorithms in ZEUS-2D (see Paper I). The great advantage of the third method is that it can be used for problems in which the analytic boundary conditions are difficult to implement properly, or even for problems for which no analytic solution exists at all.

We have used both the single-step and self-convergence testing methods to measure the convergence rate of the whole ZEUS-2D code on the one-dimensional WD problem (whereas in Paper I we measured the convergence rate of the advection algorithms alone). For both tests, we used the first WD solution (with $\gamma = 1.2$, $\Theta = 0.5$, $\omega = 0.25$) on the domain $r \in (0.5, 3.0)$ and using from 50 to 1000 radial grid points with the van Leer advection scheme. To try to remove the effects of errors at the boundaries, we ignore the first and last two grid points in both cases.
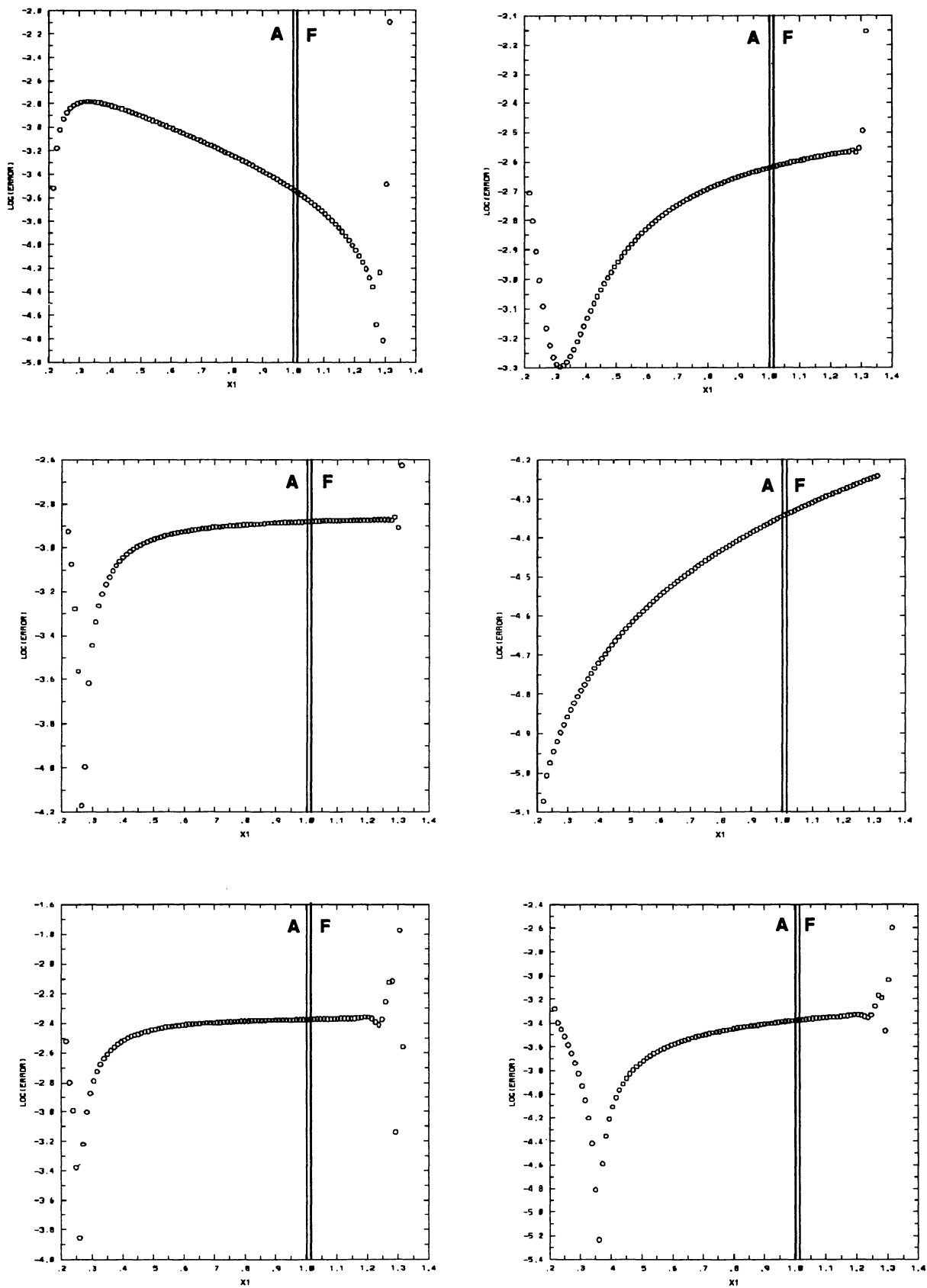
FIG. 10.—Relative errors in the Weber-Davis wind solution shown in Fig. 9

The results from the single time step convergence test are shown in Figure 11, which plots both the relative error and convergence rate for each variable. We find the asymptotic convergence rate is 1.0 for every variable except the rotational velocity, which shows no systematic trend. The results from the self-convergence test, including both the absolute errors
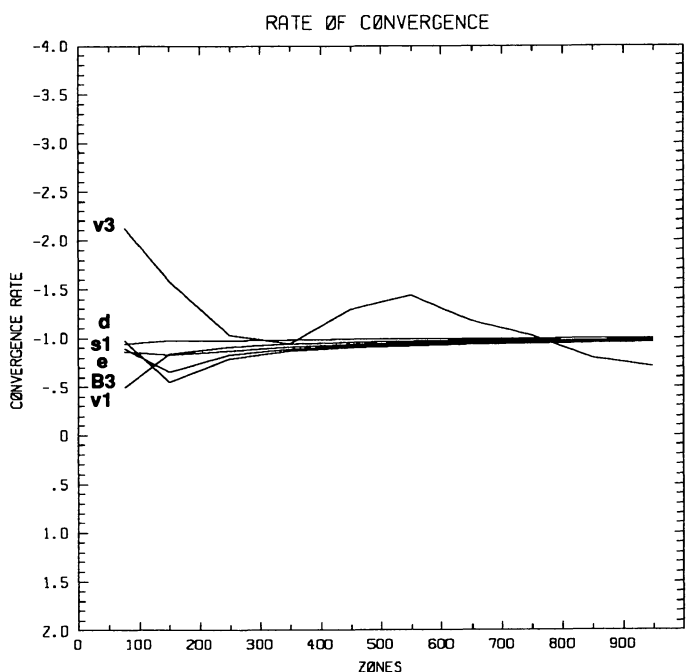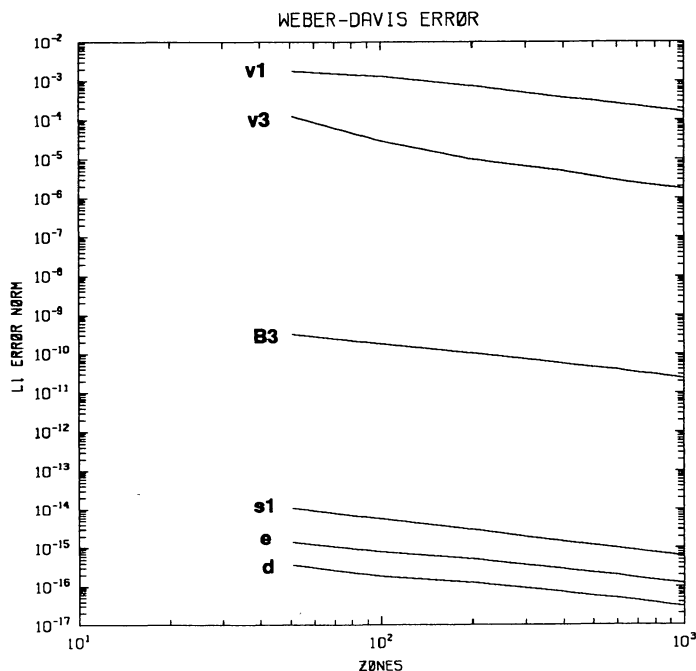

WEBER-DAVIS ERROR

RATE OF CONVERGENCE

FIG. 11.—Errors and convergence rates for each variable of the ZEUS-2D code on a one-dimensional Weber-Davis wind solution with the parameter set $\gamma = 1.2$, $\Theta = 0.5$, and $\omega = 0.25$ measured using a single-step convergence test.
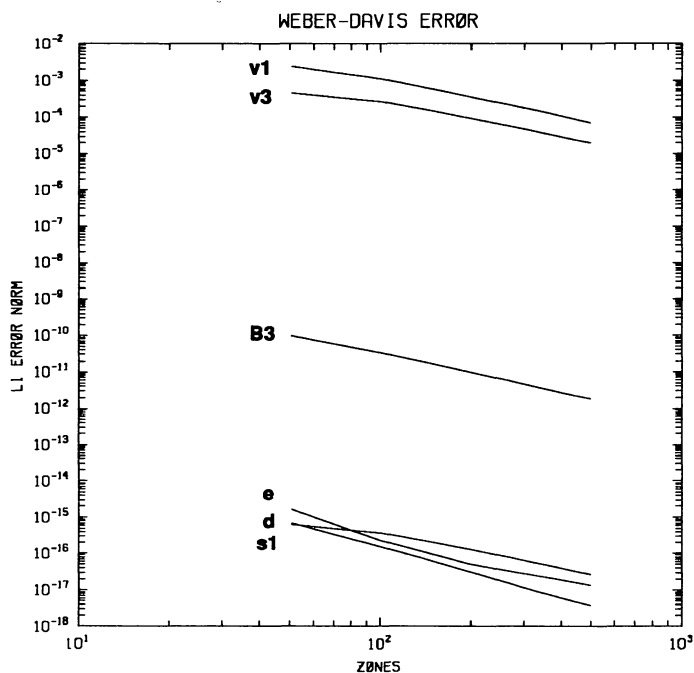
WEBER-DAVIS ERROR

RATE OF CONVERGENCE
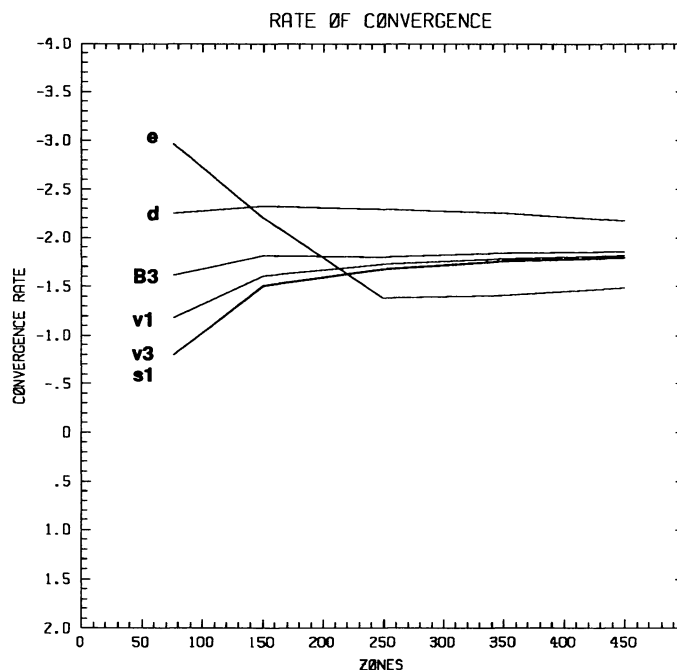
FIG. 12.—Errors and convergence rates for each variable of the ZEUS-2D code on a one-dimensional Weber-Davis wind solution with the parameter set $\gamma = 1.2$, $\Theta = 0.5$, and $\omega = 0.25$ measured using a self-convergence test.

and convergence rates, are given in Figure 12. In this case, we find the asymptotic convergence rate varies between 1.5 for e up to 2.2 for ρ. Note that we cannot run this test up to as high a resolution as the single-step test due to cpu time constraints.

The source of the discrepancy between the convergence rates measured with these two methods is uncertain. One possi-

ble explanation is that to run the WD problem, we must use a finite slice of the angular coordinate since our implementation of CT is intrinsically two-dimensional, so that both components of the poloidal field are always updated. We have used periodic boundary conditions in the polar angle coordinate, so that variations of variables in this direction will be small compared to the radial dependence. However, the finite extent of the problem in the polar angle direction may be affecting the convergence rates. Hawley (1989) reports that for a fully one-dimensional code, the single-step convergence test yields convergence rates of between 1.0 and 1.7 for all variables.

The fact that we do not achieve convergence rates of near 2 for the self-convergence test using a second-order-accurate van Leer advection scheme indicates that the error is being dominated by some step in the calculation other than the one-dimensional radial advection (which we showed in Paper I gave asymptotic convergence rates of 2.1 for the van Leer scheme). One possible source of this error is the arithmetic averaging on the staggered grid required to compute some variables (e.g., the momentum density from the mass density and velocities). Another may be that because the radial velocity is spatially varying, a velocity corrected transport scheme (Finn & Hawley 1989) which accounts for the internal structure of the velocity field within a zone must be used to achieve second-order convergence with the van Leer scheme. However, further work is required to decide this issue.

We have found that convergence testing, particularly single-step tests, are an excellent way to find subtle bugs in the coding. If the convergence rate is observed to be near zero, or very erratic for a particular variable, then this suggests a bug may be present. Moreover, with single-step evolution the convergence rates of many variables become effectively decoupled. This often allows one to identify which equation may be the source of the trouble, something not possible for nearly every other method of testing.

4.4. The Solar Coronal Transient Models of B.C. Low

To verify the multidimensional algorithms in ZEUS-2D, it is vital to perform a fully two-dimensional MHD test problem. While the two-dimensional magnetic stellar wind solutions of Sakurai (1985) are attractive, they are generated by a very complex numerical method themselves, and therefore their use as a test problem is difficult. Indeed, multidimensional stellar wind solutions are still an active area of research. We have found, however, that the analytic, time-dependent two-and three-dimensional models of solar coronal transients by Low (1984, and references therein) are excellent test problems. In fact, since Low has provided time dependent analytic solutions for a variety of physical situations, even including self gravity for the flow, and in two and three dimensions, these models may prove to be standard tests for many MHD codes in the future.

Low's (1984) models were originally constructed to study the solar coronal transients, the often violent expulsions of coronal plasma which have been revealed by the intense observational efforts directed at the solar corona over the last decade (Hundhausen 1989). The solar corona is much more active than previously thought; coronal transients may occur as often as twice a day, involving energies of 10^{31} ergs and ejecting up to

10^{15} gm of matter per event. To attempt to understand the dynamics of the solar corona, many theoretical studies, both analytic and numerical, are now underway.

Low's models are constructed by assuming that at $t = t_0$, a hot, magnetized bubble has been ejected and is being forced into a spherically symmetric, non-magnetic ambient medium. At the contact surface between the two media, a strong shock develops and runs ahead of the contact surface, heating and compressing the nonmagnetic ambient gas. Let R_S the radial position of the shock and R_C the position of the contact surface. Then at later times, the flow is characterized by three regions:

1. For $r < R_C$ the flow consists of a spherically symmetric radial outflow and an axially symmetric magnetic field. Stresses in this field are balanced by pressure gradients in an axially symmetric pressure and density distribution coincident with the spherically symmetric radial outflow.

2. For $R_C < r < R_S$ is a spherically symmetric radial outflow consisting of a shell of hot, compressed unmagnetized ambient gas.

3. For $r > R_S$ is the spherically symmetric undisturbed, non-magnetic ambient medium extending to infinity.

The spherically symmetric radial outflow in the region $r < R_S$ is generated by using the strong shock jump conditions (e.g., Courant & Friedrichs 1948) and the properties of isentropic flow. The axially symmetric magnetic medium participating in the outflow for $r < R_C$ is generated using the methods outlined by Low (1984). We do not give the details here, but merely state the results. Table 1 gives the functional form of the spherically symmetric radial outflow. Values for the parameters needed in these equations, based on the values used by Low, are given below in Table 3. Our table corrects five typographical errors in the data for the radial outflow originally presented by Low (1984, see his Table 1). The axially symmetric magnetic medium located at $r < R_C$ is generated by two arbitrary functions, one for the toroidal and one for the poloidal field components. Low studied the solutions for five specific examples of these generating functions. In our tests we have found the second set, presented in § II of Low (1984), are the most convenient. The functional form of the axially symmetric magnetic field, pressure and density resulting from these generating functions and added to the spherically symmetric radial outflow are given in Table 2; values for additional

TABLE 1

FUNCTIONAL FORM OF THE SPHERICALLY SYMMETRIC
RADIAL OUTFLOW

$r < R_C$:	$p_s(r, t) = (4\nu^3)^{-1}[GM/r]^4$
	$\rho_s(r, t) = \nu^{-3}[GM/r]^3$
	$v_r(r, t) = r/t$
$R_C < r < R_S$:	$p_s(r, t) = (7/6)\Phi^{-4}d_0\eta R_0^2 \exp[2GMR_0^6/3\eta\zeta^9]$
	$\rho_s(r, t) = 7\Phi^{-3}d_0(R_0/\zeta)^8 \exp[2GMR_0^6/3\eta\zeta^9]$
	$v_r = (r, t) = r/t$
$r > R_S$:	$\rho_s(r) = d_0(R_0/r)^{26/7} \exp[(2GM/3\eta R_0^3)(R_0/r)^{9/7})]$
	$v_r(r) = 0$

NOTES.—$\Phi = \Phi(t) = \eta^{1/2}t$, $\zeta = \zeta(t) = R_0\Phi^{1/6}$; $R_C = R_C(t) = \zeta_C\Phi$, $R_S = R_S(t) = R_0\Phi^{7/6}$; $d_0 = 10^8 m \exp[-2GM/3\eta R_0^3]$.

TABLE 2

FUNCTIONAL FORM OF THE AXIALLY SYMMETRIC
MAGNETIC MEDIUM

$$B_r(r, \theta, t) = 2A_0 r^{-2}[P_0 + (\lambda\zeta)^{1/2}J_{3/2}(\lambda\zeta)]\cos\theta$$

$$B_\theta(r, \theta, t) = -A_0\lambda(r\Phi)^{-1}[(\lambda\zeta)^{1/2}J_{1/2}(\lambda\zeta) - (\lambda\zeta)^{-1/2}J_{3/2}(\lambda\zeta)]\sin\theta$$

$$B_\phi(r, \theta, t) = A_0\lambda(r\Phi)^{-1}[P_0 + (\lambda\zeta)^{1/2}J_{3/2}(\lambda\zeta)]\sin\theta$$

$$p(r, \theta, t) = (4\pi r^4)^{-1}A_0P_0(2 - \lambda^2\zeta^2)\tilde{A}(\zeta, \theta) + p_s(r, t)$$

$$\rho(r, \theta, t) = (2\pi GMr^3)^{-1}A_0P_0(4 - \lambda^2\zeta^2)\tilde{A}(\zeta, \theta) + \rho_s(r, t)$$

NOTES.—$\tilde{A}(\zeta, \theta) = A_0[P_0 + (\lambda\zeta)^{1/2}J_{3/2}(\lambda\zeta)]\sin^2\theta$; p_s and ρ_s are given in Table 1.

parameters needed in these equations are also listed in Table 3. Note that for $r > R_S$ a value for the pressure in the unshocked ambient medium has not been specified. Since the shock is very strong, the jump conditions across the shock do not depend on the preshock pressure. Nonetheless, the preshock pressure cannot be completely arbitrary, as it must balance the gravitational attraction of the sun so that the ambient medium is in hydrostatic equilibrium. Instead, we merely ignore gravitational forces in the preshock ambient medium ($r > R_S$), rather than explicitly evaluating the pressure which gives hydrostatic equilibrium.

To run the Low model as a test, we initialize the analytic solution listed in Tables 1–3 in spherical polar coordinates on a grid of 128 radial by 80 polar zones on the domain $r \in (1 \times 10^{11}, 5 \times 10^{11})$ and $\theta \in (0, \pi)$. Note that although the Low models possess equatorial symmetry, we evolve the model over the full angular domain 0 to π to check that our numerical results can maintain this symmetry. Boundary conditions at the lower radial boundary are specified using the time-dependent analytic solution, while the outer radial boundary is outflow, and the polar angular boundaries are both axes of symmetry. The solution is evolved to a time of $t = 2.62 \times 10^4$ s, which coincides with the time of the final plot given by Low for this solution. We can compare our numerical results with the plots given by Low (his Figs. 5–7) and in addition, since the solution is analytic, we can compute the error in our numerical solution at any time. Figure 13 shows the density contours, poloidal field lines and contours of the toroidal field compo-
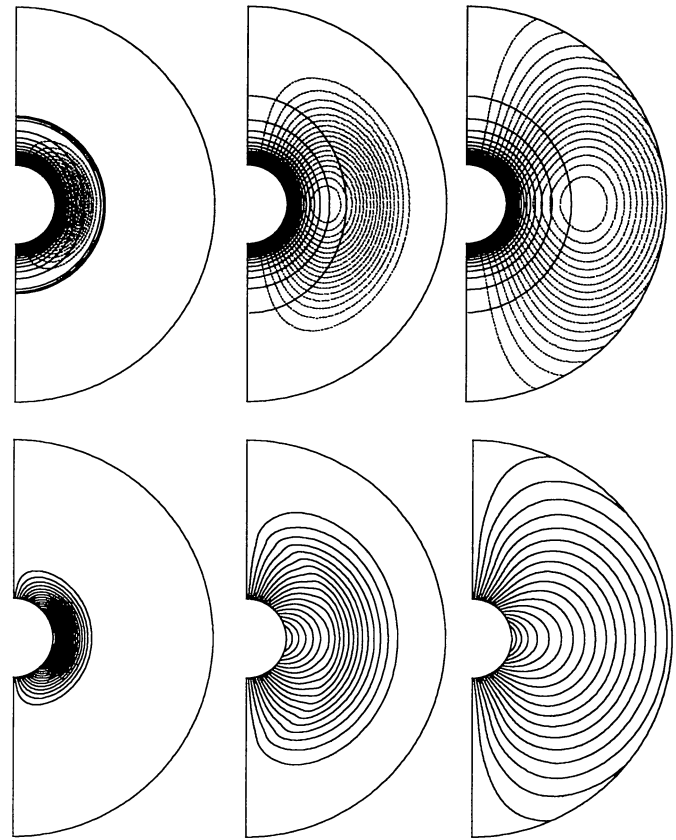
TABLE 3

VALUES FOR PARAMETERS IN LOW MODEL
(IN cgs UNITS)

Parameter	Value
λ	5.54×10^{11} cm^{-1}
A_0	1.5×10^{21} G cm^2
P_0	1.01327
ζ_C	1.104×10^{11} cm
η	5.24×10^{-8} s^{-2}
ν	2.42×10^{20} cm^3 s^{-2} g$^{-1/3}$
G	6.67×10^{-8} cm^3 s^{-2} g^{-1}
M	2.0×10^{33} gm
m	1.673×10^{-24} gm
R_0	1.0×10^{11} cm
t_0	8.74×10^3 s

FIG. 13.—Numerical solution of the coronal transient problem due to B.C. Low as computed by ZEUS-2D. The top panels show contours of the density (*solid lines*) overlaid representative field lines projected into the poloidal plane. The bottom panel shows contours of the toroidal component of the field. Plots are shown at dimensionless times of $\Phi = 2, 4,$ and 6, where Φ is defined in Table 1. Sixteen equally spaced contours between the maximum and minimum are shown.

nents at three different times during the evolution. We find the numerical solution agrees well with the analytic solution. Physically, a magnetic bubble is ejected from the corona, preceded by the shock and contact discontinuity. At the final time, both the shock and contact discontinuity have left the grid. In Figure 14, we provide a more quantitative check by presenting the relative errors for the density, energy, radial velocity and toroidal magnetic field at the termination of the calculation. We find the errors are dominated by two features, a wave of error which has been generated by the inability of the numerical solution to properly represent the discontinuities present in the solution at $t = t_0$, and a large error in the last radial zone associated with the outflow boundary conditions. The error generated in the initial discontinuities cannot be easily eliminated: it is a consequence of trying to represent a mathematical discontinuity with a finite numerical resolution. We have encountered it previously whenever we performed tests involving shocks. The error at the outer boundary, however, indicates the ineffectiveness of our outflow boundary conditions at propagating submagnetosonic flows. Clearly, improvements may be needed here for some problems.
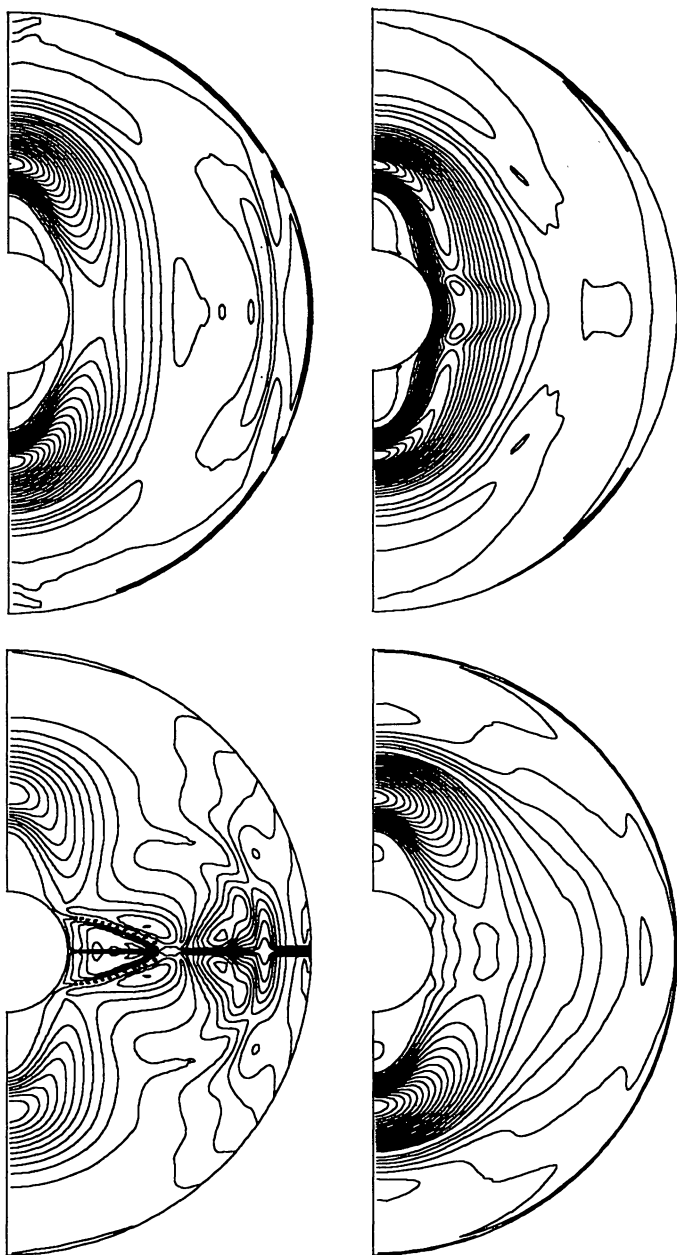
FIG. 14.—Relative errors in the density (*top left*), radial velocity (*top right*), and radial and toroidal components of the magnetic field (*bottom left and right, respectively*) in the numerical solution to the coronal transient problem as computed by ZEUS-2D at time $\Phi = 6$. The maximum errors in each case are 6.16%, 6.86%, 3.07%, and 9.46%. Sixteen equally spaced contours between the maximum and minimum are shown.

4.5. *Magnetic Braking of an Aligned Rotator*

The next MHD test of the ZEUS-2D code we have performed is the magnetic braking of an aligned rotator. The problem is defined by a homogeneous cylinder of gas of density ρ_d located in a homogeneous ambient medium with density ρ_x. Both the disk and the ambient medium are threaded by a uniform strength axial magnetic field with magnitude B_0. At $t = 0$, the disk is given a constant angular velocity. This pro-

duces shearing motion at the surface of the disk, which generates torsional Alfvén waves that propagate along the field lines both into the ambient medium (accelerating it) and into the disk (decelerating it). The solution to the problem gives the evolution of the angular velocity of the disk and the ambient medium by describing the propagation of the torsional Alfvén waves. Mouschovias & Paleologou (1980, hereafter MP) have given an exact, time-dependent analytic solution to this problem, making it an excellent candidate for the testing of the ability of ZEUS-2D to propagate torsional Alfvén waves.

The analytic solution given by MP is given in terms of dimensionless units, so that $B_0 = 1$, $\rho_x = 1$, and lengths are measured in units of $Z =$ half thickness of disk $= 1$. Time is then measured in units of the Alfvén crossing time of the disk, using the Alfvén speed in the ambient medium. A single dimensionless parameter ($\alpha = \rho_d/\rho_x = \rho_d$ in dimensionless units) determines the magnetic braking time of the cloud and characterizes the solutions. These solutions can be understood most readily by using spacetime diagrams to trace the evolution of the Alfvén waves. Figure 15 shows two such diagrams, one for the case $\rho_d = \rho_x$, and one for the case $\rho_d > \rho_x$. In the former case, the density is continuous across the surfaces of the disk,
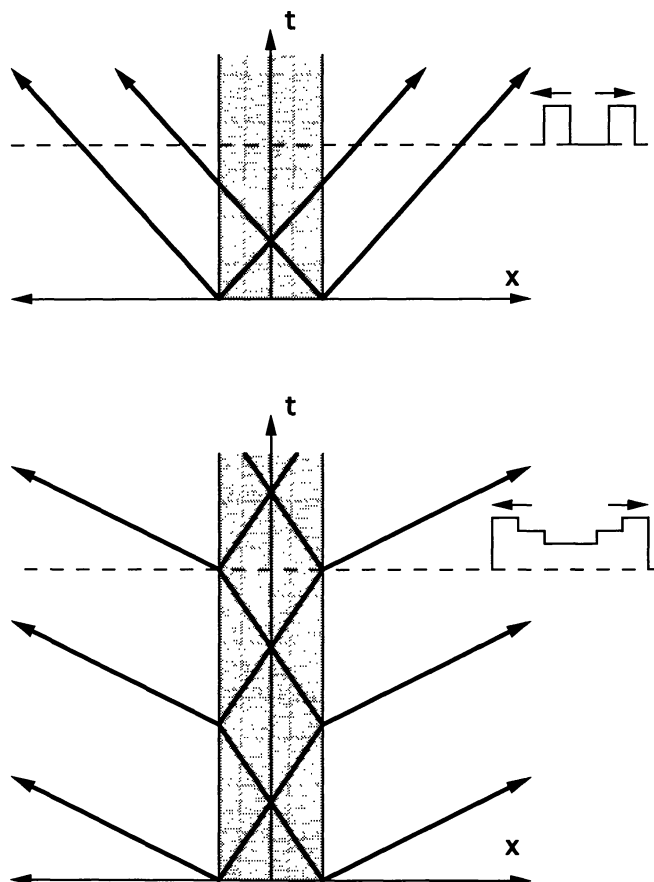

FIG. 15.—Spacetime diagrams of the evolution of the solution to the magnetic braking of an aligned rotator test problem for a disk to external medium density ratio of 1 (*top*) and greater than 1 (*bottom*). The latter case is characterized by internal reflections at the surface of the disk (*shaded region*). Along a particular time slice are shown typical wave patterns in each case.

and the torsional Alfvén waves generated at the two disk surfaces propagate to infinity without reflections. At any time slice, the solution consists of two square pulses of rotational velocity and magnetic field propagating away from each other at the Alfvén speed. In the latter case, the solution is complicated by the internal reflections of Alfvén waves that occur at the disk surface (for a density discontinuity, the associated reflection coefficient for a torsional Alfvén wave is $\mathscr{R} = [\alpha^{1/2} + 1]/[\alpha^{1/2} - 1]$). The partial transmissions that occur at each internal reflection generate a new wavefront, which propagates out into the external medium. At any time slice, the solution consists of a stair step of these wavefronts, with the number of steps determined by the number of internal reflections that have occurred in the disk. The mean angular velocity of the disk decreases exponentially in time, with a characteristic magnetic braking time of $t_{MB} = (\rho_d/\rho_x)(Z/v_{A,ext})(t_{MB} = \alpha$ in di-

mensionless units). MP give the full time-dependent, analytic solution for both of these cases, and using a discontinuous initial condition (DIC) for the rotational velocity at the surface of the disk, and a continuous initial condition (CIC) in which the rotational velocity drops smoothly to zero in the ambient medium following a cosine function. In Stone et al. (1992) FORTRAN subroutines are given to compute the MP analytic solution for both DIC and CIC.

Using the MOC algorithm in ZEUS-2D, we have performed the magnetic braking test problem with several values for the density ratios and using both the DIC and CIC. We use very small amplitudes for the torsional waves to prevent gradients in the toroidal field from generating compressive waves which interfere with the subsequent evolution. Figure 16 shows the results for a density ratio of 10, using the DIC and both the van Leer and PPA interpolation algorithms for the MOC update. A
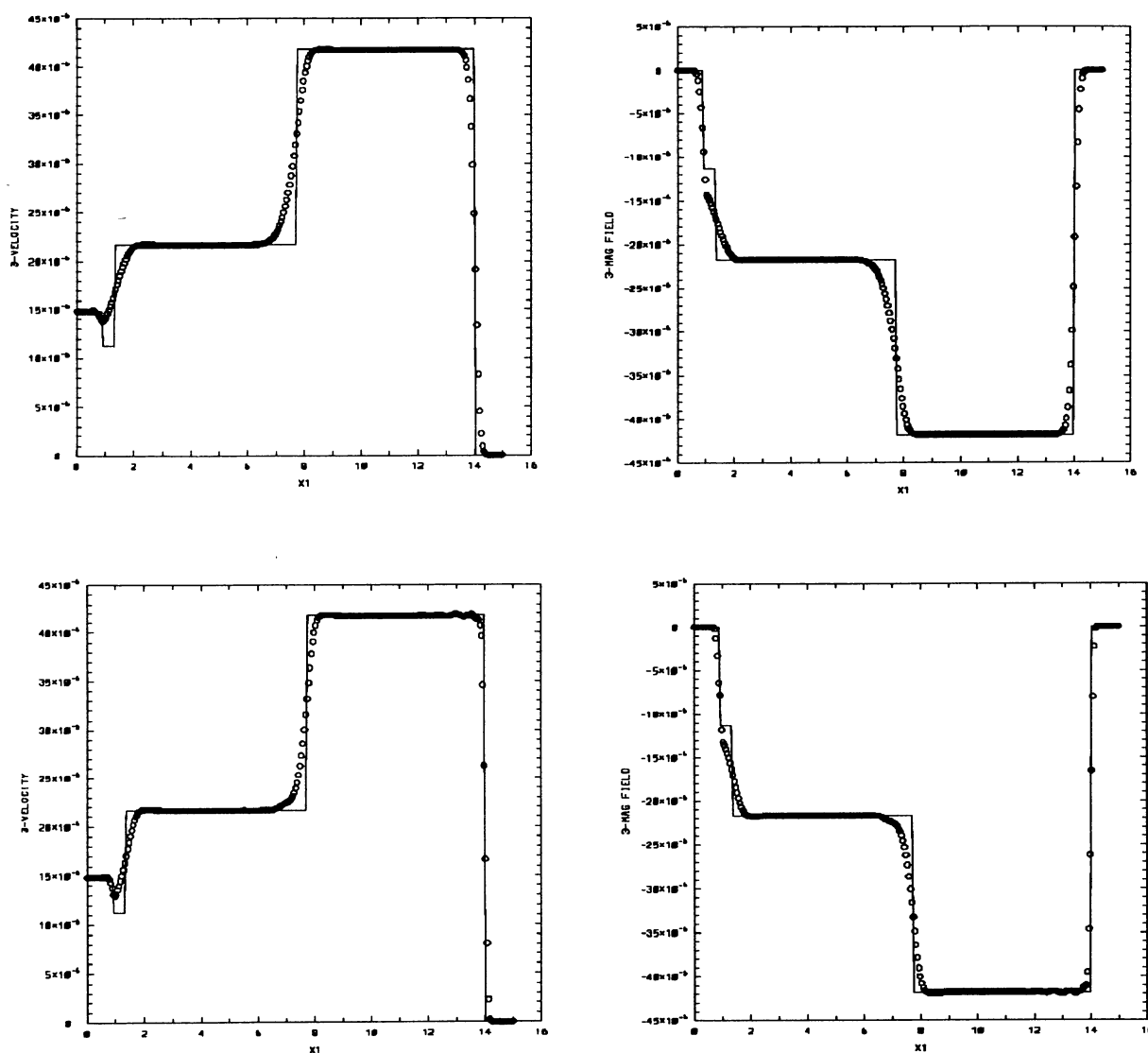

FIG. 16.—Results for the magnetic braking of an aligned rotator test problem starting from discontinuous initial conditions (DIC) and using the van Leer (top) or PPA (bottom) interpolation algorithms in the MOC update for the torsional velocity and magnetic field. The analytic solution is plotted as a solid line, while the numerical solution generated by ZEUS-2D is shown as points. The density ratio in the of the disk (located at $x < 1$) to the ambient medium is 10 in both cases.

grid of 300 zones is used on the domain $z \in (0, 15)$, so that 20 zones are located in the disk at $z < 1$. The evolution is stopped at $t = 13$, just before the first wavefront leaves the grid. The results show the numerical solution gives excellent agreement with the analytic solution (*solid line*) for both the rotational velocity and toroidal magnetic field. The number of zones representing the discontinuities is consistent with the performance of the interpolation algorithms on advection problems, i.e., the van Leer method smears the discontinuities over about 14 zones, while PPA (with no steepener) keeps them to about six. We reiterate that of the schemes we tested, the MOC is the only method that produces suitable results to this problem. We find that straightforward finite differencing of the coupled toroidal terms in the equation of motion and induction equation leads to an unacceptable dispersion error. Only schemes which

have a large intrinsic diffusion (such as Lax-Friedrichs or Lax-Wendroff) are able to damp this error away, however these schemes are therefore unable to resolve sharp features in the flow.

Figure 17 shows the results for the same problem, but using the CIC instead. Again, we find excellent agreement between the numerical and analytic solutions. The van Leer scheme does not resolve the minima in the angular velocity correctly, whereas the higher order PPA scheme does. The most important feature of Figure 17, however, is that the evolution has been stopped at a later time ($t = 15$), so that the initial wavefront has already left the grid. However, we note there is no reflection of the wave via the outflow boundary condition, i.e., using the MOC evolution of the torsional Alfvén wave, we can achieve perfectly transparent outflow boundary conditions for
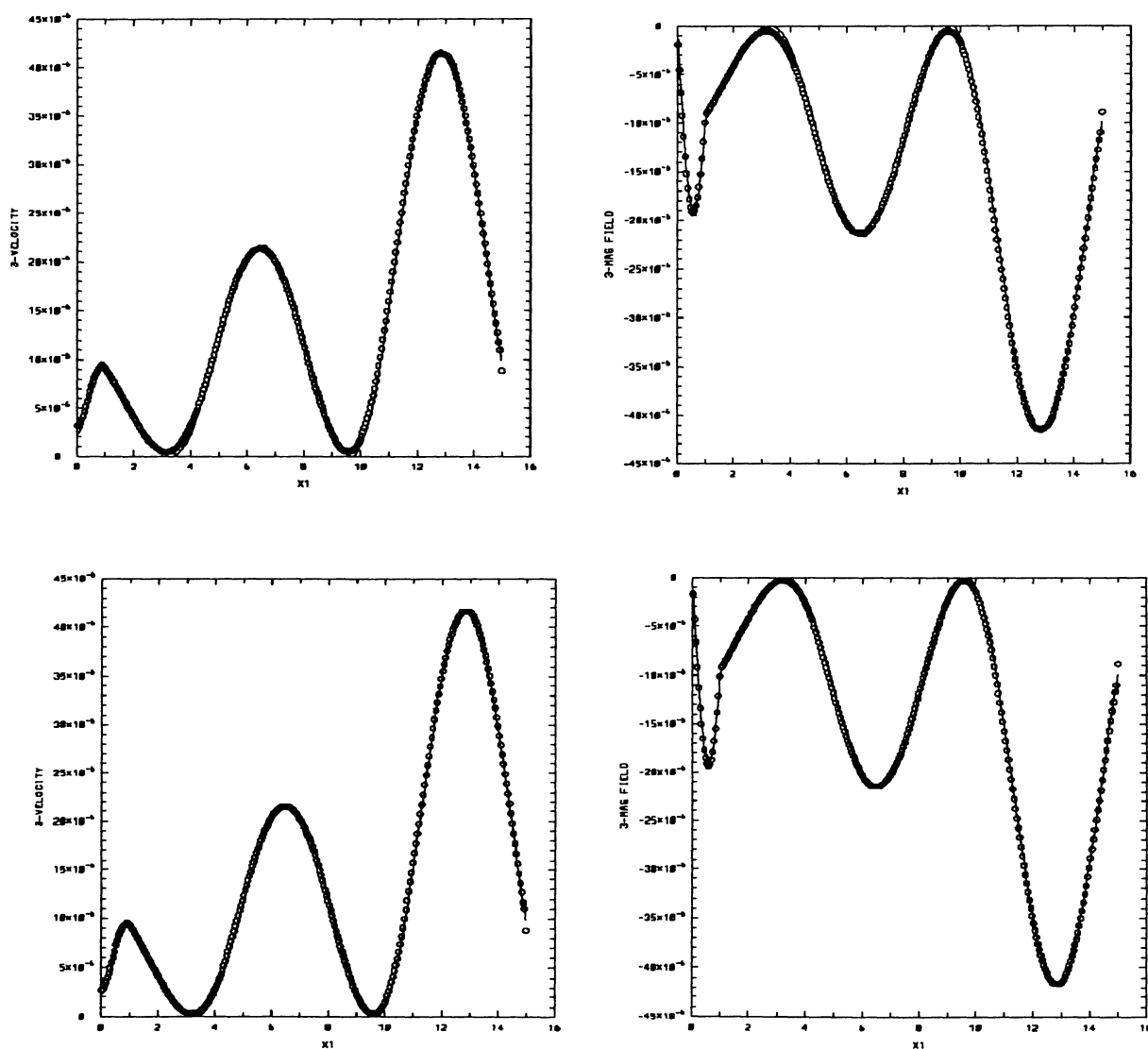

FIG. 17.—Results for the magnetic braking of an aligned rotator test problem starting from continuous initial conditions (CIC) and using the van Leer (*top*) or PPA (*bottom*) interpolation algorithms in the MOC update for the torsional velocity and magnetic field. The analytic solution is plotted as a solid line while the numerical solution generated by ZEUS-2D is shown as points. The density ratio in the of the disk (located at $x < 1$) to the ambient medium is 10 in both cases.

these waves. This is an important and happy consequence of using upwind differencing for the torsional Alfvén wave terms.

As an additional test, we have investigated whether the diffusivity of the interpolation algorithms (as manifested by the smearing of discontinuities) interferes with the ability of the numerical solution to follow the exponential decay of the angular velocity of the disk properly. We have tested this using a very large density ratio for the disk (to give a long magnetic braking time), and have followed the evolution for many braking times. We find the MOC follows the exponential decay very well. Finally, an additional important question is whether or not the directionally split implementation of the MOC we have implemented for the toroidal field components gives accurate results in two-dimensional problems. To test this, we have repeated the magnetic braking test problem in spherical polar coordinates. Since the Alfvén waves follow the axial magnetic field, they will propagate across grid lines rather than along them (as in cylindrical geometry), and the outgoing waves will encounter a curved outer boundary. Nonetheless, we find our method propagates the waves axially, with no evidence for polar motion along the curved grid lines. In addition, the waves are transmitted through the outer boundary clearly, with no signs of reflection.

4.6. Propagation of Shear Alfvén Waves

The necessity of using the MOC update for evolving torsional Alfvén waves originally led us to develop the MOC-CT scheme as described in § 3.2 for evolving the poloidal field. To demonstrate the necessity of the use of the MOC-CT scheme, we can use the poloidal (shear) analog of the magnetic braking of an aligned rotator problem. In Cartesian geometry, if the "disk" (i.e., the region $x < 1$) is given an initial shear motion in the orthogonal direction to the field lines (rather than a toroidal motion as in cylindrical geometry), then the problems (and their solutions) are identical. Thus, we can use the analytic solutions of MP to test the propagation of shear Alfvén waves along the poloidal field lines.

Figure 18 shows the results of propagating a shear wave in the 1-direction with DIC for a density ratio of one using the original method of computing the EMF in the CT scheme as described by EH. This method does not use the MOC to upwind along Alfvén wave characteristics, but simply upwinds the magnetic field components using the fluid velocity. The large dispersion error present in this method is clearly evident, indeed the result is nearly identical to those we first achieved with the original, straightforward finite-differencing scheme of the toroidal field. The results of this test, combined with our experiences in finding an accurate algorithm for propagating the toroidal waves, led us to develop the MOC-CT scheme for evolving the poloidal field described in § 3.2.2. This scheme reduces to the MOC used for the toroidal field if $v = 0$, whereas if $v_A = 0$ it reduces essentially to the original method. Figure 19 gives the results for the identical problem with the MOC-CT scheme for both a stationary ($v_x = 0$) and a moving fluid ($v_x = 1.5$). The former case is identical to the toroidal test problem, and we find identical results. The MOC-CT scheme clearly now provide for an accurate evolution of shear waves. In the case that the fluid is moving, the wave fronts should propagate at $v = v_x \pm v_A$, which since we have used $v_A = 1.0$ should give $v = 0.5$ for left-going waves and $v = 2.5$ for right-going waves.
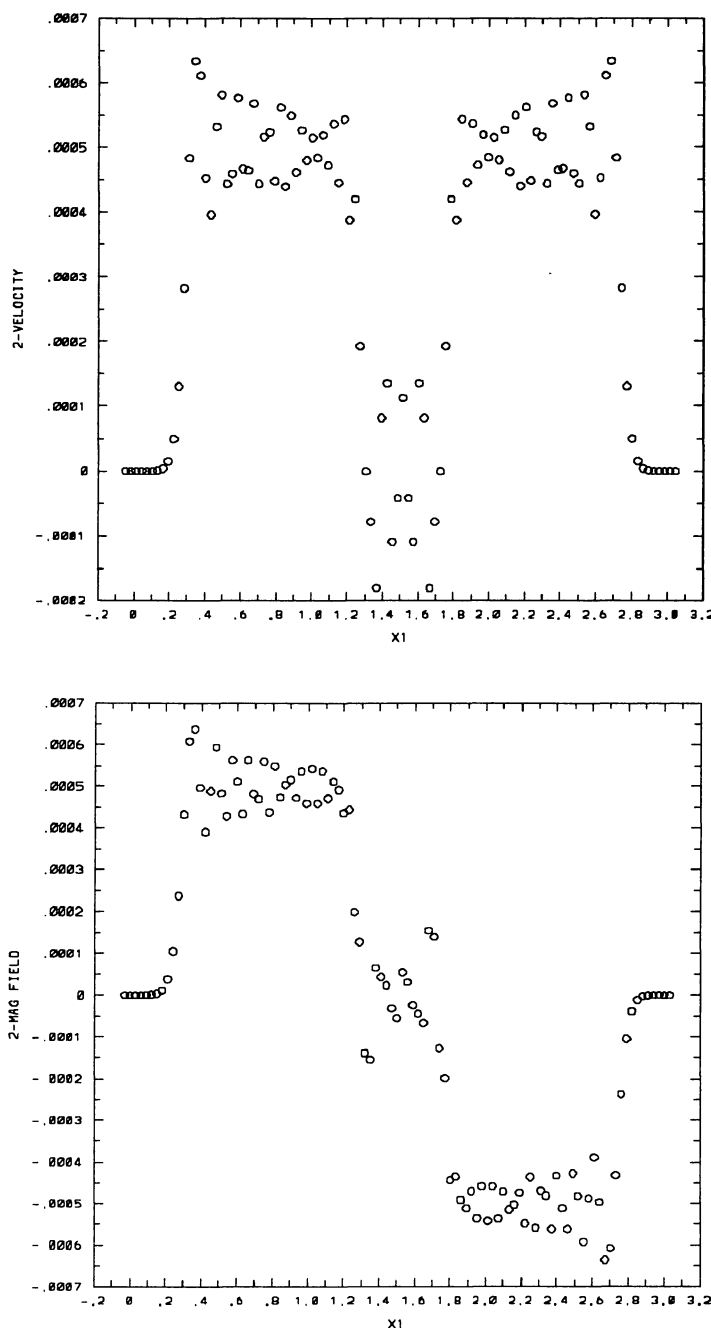

FIG. 18.—Propagation of a shear Alfvén wave using the original method for computing the EMF in the CT formalism as described by EH. Initially, the 2-velocity is perturbed in the region $1 < x < 2$, which should result in two square pulses of 2-velocity (*top*) and 2-magnetic field (*bottom*) traveling in opposite directions along the 1-magnetic field lines. The method is clearly unable to propagate the shear Alfvén waves accurately in this test.

Our test solution propagates wave pulses through the moving fluid at the correct characteristic speeds.

5. SUMMARY

In this paper we have given a detailed description of the MHD algorithms used in the ZEUS-2D code. These algorithms are based on the CT formalism of EH to ensure diver-

gence free evolution of the magnetic field, and the MOC to insure accurate propagation of Alfvén waves.

In addition to a description of the algorithms, we have also presented the results of the MHD test problems performed on ZEUS-2D. In order to enable other researchers to use these same test problems to calibrate other codes, we present a more detailed description of the setup and execution of each test problem in Stone et al. (1992).

The Cartesian advection tests, used mainly to check for coding bugs, reproduce the same quality of results as were achieved for the HD advection tests using the same advection algorithms. However, unlike some MHD algorithms based on evolving the vector potential, the CT scheme produces monotonic profiles for the electric current densities. With the MHD Riemann problem, we discovered the algorithms in ZEUS-2D can accurately trace the new types of wave modes that can be present in MHD flows (e.g., compound waves). Comparisons of the HD and MHD Riemann problems reveals the much

greater complexity of the latter problem. The one-dimensional magnetic stellar wind solutions of Weber and Davis are an excellent way of checking the coupling of the velocity and magnetic field components in a rotating outflow. We have also used the Weber-Davis problem to perform convergence testing of the full ZEUS-2D code. This convergence testing reveals that the full code generates solutions which converge at less than second order. Further work is needed to identify the dominant source of error at higher resolutions which is limiting the convergence rate. As a general technique, we feel convergence testing can be an excellent way to quantify the overall performance of a hydrocode, and can help to find subtle bugs in coding. The only two-dimensional MHD test problem we have performed is the coronal transient test problem due to Low (1984). We find the agreement between our numerical results and Low's analytic solutions are excellent. These two- and three-dimensional solutions should prove useful as a standard for testing multidimensional MHD codes in the future.
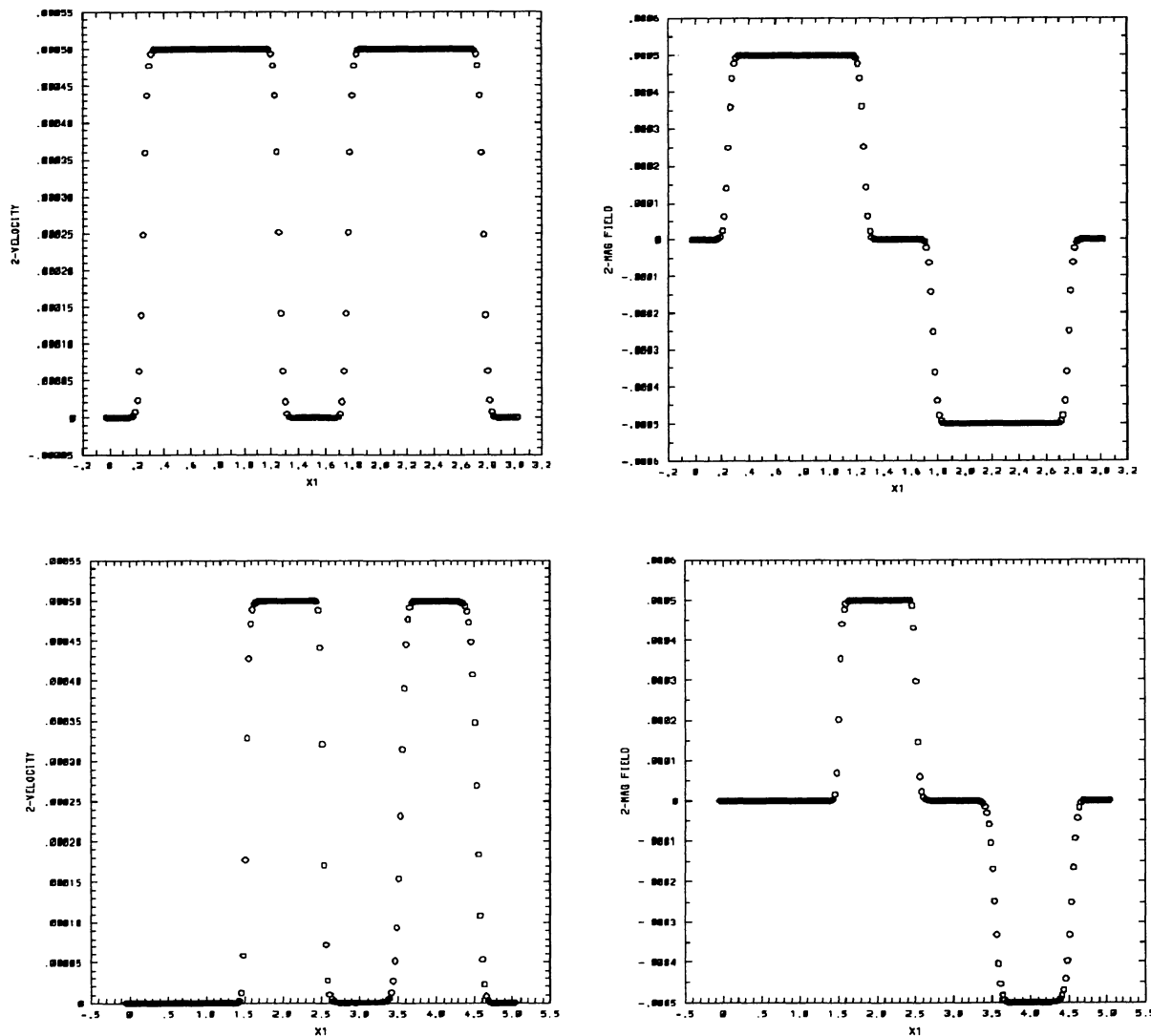

FIG. 19.—Propagation of a shear Alfvén wave using the MOC-CT scheme for a stationary (top) and a moving (v = +1.5 bottom) fluid. Initially the 2-component of the velocity is perturbed in the region 1 < x < 2 for the former, and 2 < x < 3 for the latter, which generates two square pulses of 2-velocity (left) and 2-magnetic field (right) traveling in opposite directions along the magnetic field lines.

One of the most important test problems we have performed is the magnetic braking of an aligned rotator, which allows us to check the ability of ZEUS-2D to propagate nonlinear Alfvén waves. Of the methods we tested, we found the only suitable scheme for propagating steep nonlinear Alfvén waves was based on the MOC. All other methods either possess an unacceptable dispersion error (e.g., schemes which are upwind in the fluid velocity only) which results in large amplitude short-wavelength oscillations, or are simply too diffusive (e.g., Lax-Wendroff). Indeed, one solution to the dispersion error is to add large amounts of diffusion. Instead, we have shown that our MOC scheme for evolving the toroidal magnetic field and velocity components can accurately propagate torsional Alfvén waves with little diffusion. Similarly, the MOC-CT scheme we have developed for evolving the poloidal field com-

ponents can propagate poloidal Alfvén waves equally well. These tests indicate that the MOC-CT scheme described in § 3.2.2 is important and necessary improvement for the accurate evolution of all MHD wave modes. It is hoped that the algorithms described here will provide a solid foundation for future numerical MHD calculations.

REFERENCES

Brio, M., & Wu, C. C. 1988, JCP, 75, 400 (BW)
Choptuik, M. W. 1986, Ph.D. thesis, Univ. British Columbia
Clarke, D. A. 1988, Ph.D. thesis, Univ. New Mexico
Clarke, D. A., Norman, M. L., & Burns, J. O. 1986, ApJ, 311, L63
———. 1989, ApJ, 342, 700
Clarke, D. A., Stone, J. M., & Norman, M. L. 1990, BAAS, 22, 801
Courant, R., & Friedrichs, K. O. 1948, Supersonic Flow and Shock Waves (Berlin: Springer)
Evans, C., & Hawley, J. F. 1988, ApJ, 33, 659 (EH)
Finn, L. S., & Hawley, J. F. 1989, unpublished
Hawley, J. F. 1989, private communication
Hundhausen, A. J. 1989, preprint
Jackson, J. D. 1975, Classical Electrodynamics (New York: Wiley)
Lou, Y. Q., Rosner, R., & Ulmschneider, P. 1987, ApJ, 315, 349
Low, B. C. 1984, ApJ, 281, 392

Mouschovias, T. Ch., & Paleologou, E. V. 1980, ApJ, 237, 877 (MP)
Press, W. M., Flannery, B. P., Teukolsky, S. A., & Vetterling, W. T. 1986, Numerical Recipes (Cambridge: Cambridge Univ. Press)
Sakurai, T. 1985, A&A, 152, 121
Spitzer, L., Jr. 1962, Physics of Fully Ionized Gases, 2d ed. (New York: Wiley)
Stone, J. M. 1990, Ph.D. thesis, Univ. Illinois, Urbana-Champaign
Stone, J. M., Hawley, J. F., Evans, C., & Norman, M. L. 1992, ApJ, in press
Stone, J. M., Mihalas, D., & Norman, M. L. 1992, ApJS, 80, 819 (Paper III)
Stone, J. M., & Norman, M. L. 1992, ApJS, 80, 753 (Paper I)
Thompson, K. W. 1987, JCP, 68, 1
Vanajakshi, T. C., Thompson, K. W., & Black, D. C. 1989, JCP, 84, 343
Weber, E. J., & Davis, L., Jr. 1967, ApJ, 148, 217 (WD)